



Kinetic assessment of the dry reforming of methane over a solid solution Ni–La oxide catalyst

Víctor Stivenson Sandoval–Bohórquez,¹ Edgar M. Morales–Valencia,¹  Carlos O. Castillo–Araiza,³ Luz M. Ballesteros–Rueda,¹ Víctor G. Baldovino–Medrano*^{1,2}, 

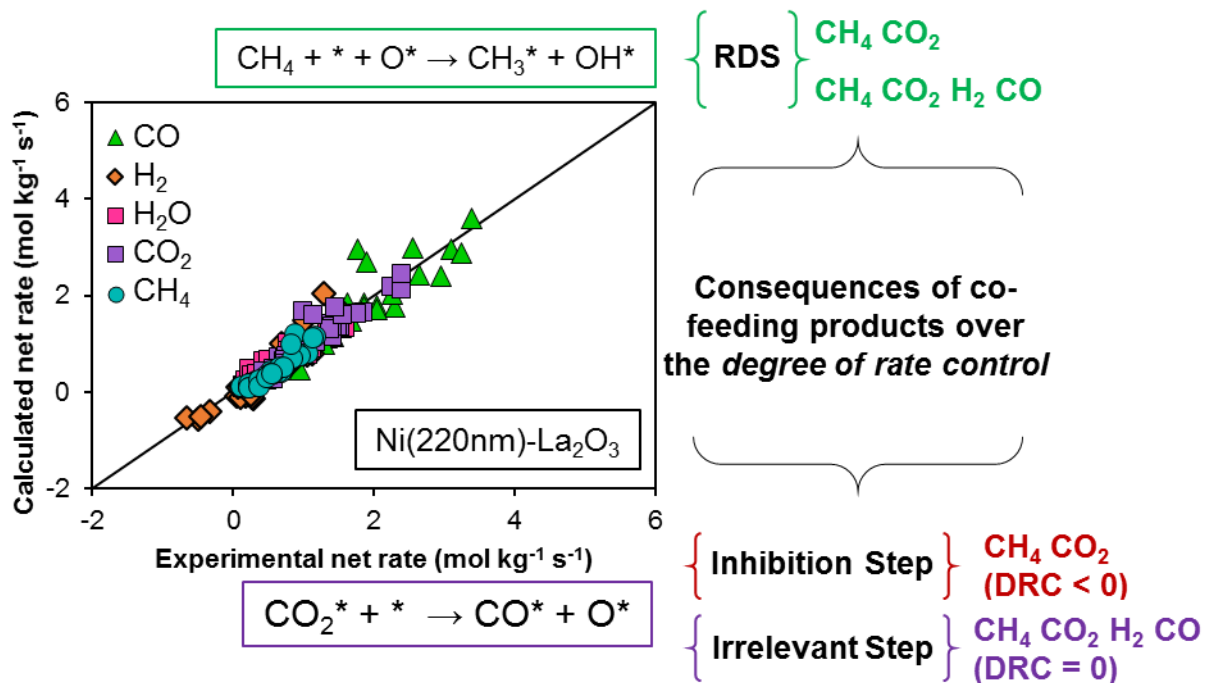
¹Centro de Investigaciones en Catálisis (@CICAT UIS) and ²Laboratorio de Ciencia de Superficies (#SurfLab–UIS), Parque Tecnológico Guatiguará (PTG), Km. 2 vía El Refugio, Universidad Industrial de Santander, Piedecuesta (Santander), 681011, Colombia.

³Laboratorio de Ingeniería de Reactores Aplicada a Sistemas Químicos y Biológicos, Departamento de Ingeniería de Procesos e Hidráulica, Universidad Autónoma Metropolitana–Iztapalapa, CDMX, Mexico.

*Corresponding author. Tel.: +57 6344000 Ext. 1485

E–mail: vicbaldo@uis.edu.co

Graphical abstract



Abstract

The dry reforming of methane is a promising technology for the abatement of CH₄ and CO₂. Solid solution Ni–La oxide catalysts are characterized by their long–term stability (100h) when tested at full conversion. The kinetics of dry reforming over this type of catalysts has been studied using both power law and Langmuir–Hinshelwood based approaches. However, these studies typically deal with fitting the net CH₄ rate hence disregarding competing and parallel surface processes and the different possible configurations of the active surface. In this work, we synthesized a solid solution Ni–La oxide catalyst and tested six Langmuir–Hinshelwood mechanisms considering both single and dual active sites for assessing the kinetics of dry reforming and the competing reverse water gas shift reaction and investigated the performance of the derived kinetic models. In doing this, it was found that: (1) all the net rates were better fitted by a single–site model that considered that the first C–H bond cleavage in methane occurred over a metal–oxygen pair site; (2) this model predicted the existence of a nearly saturated nickel surface with chemisorbed oxygen adatoms derived from the dissociation of CO₂; (3) the dissociation of CO₂ can either be an inhibitory or an irrelevant step, and it can also modify the apparent activation energy for CH₄ activation. These findings contribute to a better understanding of the dry reforming reaction's kinetics and provide a robust kinetic model for the design and scale–up of the process.

Keywords: *Solid solution Ni–La oxide catalyst, dry reforming of methane, kinetic modelling, Ni–O active site.*

1. Introduction

The conversion of the two most abundant greenhouse gases, CO₂ and CH₄, into commercially valuable syngas, i.e., a mixture of CO and H₂, via the dry reforming of methane (CH₄ + CO₂ ⇌ 2H₂ + 2CO, ΔH_{298K}⁰ = 247.3kJ.mol⁻¹, ΔG_{298K}⁰ = 170.9kJ.mol⁻¹) remains a promising technology for mitigating climate change. The reaction yields a H₂:CO molar ratio equal to unity which is adequate for the synthesis of methanol, dimethyl ether, and Fisher–Tropsch derived hydrocarbons.^{1,2} Moreover, the reaction offers the possibility to exploit methane deposits that contains significant amounts of CO₂ as well as methane from anaerobic digestion.^{3,4}

In general, the dry reforming of methane competes with parallel reactions such as the reverse water–gas shift reaction or RWGS (H₂ + CO₂ ⇌ CO + H₂O, ΔH_{298K}⁰ = 41.2kJ.mol⁻¹, ΔG_{298K}⁰ = 28.6kJ.mol⁻¹) which lowers H₂:CO molar ratios, methane dehydrogenation (CH₄ ⇌ C + 2H₂, ΔH_{298K}⁰ = 74.9kJ.mol⁻¹, ΔG_{298K}⁰ = 50.8kJ.mol⁻¹) and the so-called Boudouard reaction (2CO ⇌ C + CO₂, ΔH_{298K}⁰ = -172.5kJ.mol⁻¹, ΔG_{298K}⁰ = -120.1kJ.mol⁻¹). The latter two reactions are the sources of the chemisorbed carbon adatoms required for the diffusion and growth of carbon nanotubes.^{5,6} As shown in **Figure 1**, thermodynamically, dry reforming is promoted by a temperature increase and it prevails over its competing reactions at temperatures higher than 923K. However, the competing reactions are significant up to about 1173K,^{7,8} with which the formation of water and carbon are virtually inevitable at the typical operational temperatures (873–1073K).

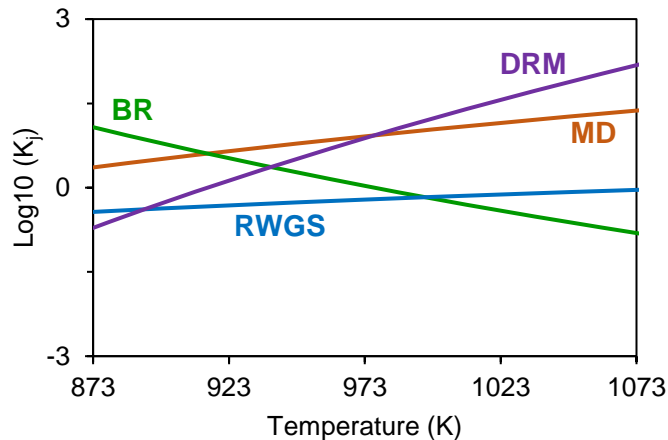


Figure 1. Logarithm of the equilibrium constant (K_j) at different temperatures. Dry reforming of methane (DRM), RWGS, methane dehydrogenation (MD), and Boudouard reaction (BR). The equilibrium constants were estimated with Aspen Plus® (AspenTech) using a Gibbs reactor model and the ideal gas package.

Nickel-based catalysts are the most studied catalysts for dry reforming due to their high activity and lower cost compared to noble metals. Conventional catalysts consisting of supported nickel nanoparticles are prone to deactivation by coking due to the formation of carbon nanotubes because of the high carbon solubility (2.03atom % at 1270K) and diffusion rate in nickel.^{9,10} In fact, carbon nanotubes can grow either on top of the nickel nanoparticles, tip-growth, or on the interface between the metal nanoparticle and the support, base-growth, depending on both the operational conditions and the metal particle size and shape.¹⁰ The tip-growth of carbon nanotubes obstructs both the active sites and the pore network of the support, while the base-growth of carbon nanotubes pushes the metal nanoparticles away from the support hence destroying the catalyst and further plugging the reactor. Most strategies employed to reduce the coking degree of Ni-based catalysts focus on increasing the concentration of surface oxygen by alloying nickel with other metals, e.g., Ni-Co,¹¹ and Ni-Fe,¹² using oxide supports with high mobility of oxygen, e.g., CeO₂,^{3,13} ZrO₂,^{2,14} MnO,⁵ or by using an oxide support able to generate carbonate-type species, e.g., CaO,^{15,16} La₂O₃,¹⁷⁻¹⁹ and Sm₂O₃.²⁰ Among the latter oxides, it is known that La₂O₃ reacts with CO₂ to form

$\text{La}_2\text{O}_2\text{CO}_3$ via acid–base interactions which may promote the removal of carbon species from the metal surface towards the metal– $\text{La}_2\text{O}_2\text{CO}_3$ interphase.^{17–19,21–25} Therefore, this type of catalyst has raised considerable interest for the development of a scalable technology involving dry reforming. Particularly, Ni– La_2O_3 formulations obtained via the solid–state thermal decomposition of perovskite precursors (e.g., LaNiO_3 , La_2NiO_4) have been investigated since this synthesis route can increase the metal–support interaction, hence alleviating the sintering/agglomeration of nickel that is considerable at temperatures above 863K.^{17,23,24,26}

Several investigations have been devoted to the kinetics of the dry reforming of methane over Ni–based catalysts using either power–law^{27–30} or Langmuir–Hinshelwood based models.^{4,31–35} In general, it has been considered that the reaction involves the following key steps:^{4,34,36} (1) the cleavage of the C–H and C–O bonds of CH_4 and CO_2 , respectively; (2) the formation of products (namely, CO, H_2 , H_2O) via surface reaction of intermediates derived from the reactant activation, e.g., chemisorbed C, H, O, OH species; and, (3) the desorption of products. The models usually consider that either the cleavage of the C–H bond in methane or another specific surface reaction can be the rate–determining step (RDS). The models also assume the existence of different types of active sites; particularly, a metallic single–site or a pair of sites located at the metal and at the support have been considered. Other approaches have also considered that one or more chemisorbed species are the most abundant surface intermediate (MASI).^{4,31–35} Given such a diversity of approaches, a substantial number of alternative and often discordant kinetic models for methane dry reforming exist.³⁴

Concerning solid solution Ni–La₂O₃ catalysts, the catalytic cycle for the dry reforming of methane is commonly described by the following reaction steps.^{19,25,29,35,37}

R1: CH₄ + * \rightleftharpoons CH₄*; CH₄ adsorption on Ni–sites denoted hereafter as *.

R2: CH₄* → C* + 2H₂: dehydrogenation of methane leading to chemisorbed C atoms.

R3: CO₂ + La₂O₃ \rightleftharpoons La₂O₂CO₃: formation of lanthanum oxycarbonate.

R4: La₂O₂CO₃ + C* → 2CO + La₂O₃ + *: decomposition of the oxycarbonate species to oxidize the chemisorbed C atoms over Ni–sites for the renewal of the metallic active site.

The kinetic models derived in the literature from such a reaction pathway are summarized in

Table 1. These expressions were developed by assuming that **R2** and **R4** are rate-determining and that the net rate of the chemisorbed C atoms equals zero, i.e., **R2** – **R4** = 0. In general, the models differ from each other depending on the considered MASI over both the metal and support sites. Besides the disagreements stemming from the latter consideration, one of the critiques that may be posed over these studies is that none of them presented estimations of all kinetic and adsorption parameters. Indeed, some of the authors included in **Table 1**,^{37,38} fed their models with parameters taken directly from the literature, and this led to inconsistencies such as the determination of high activation energies (172–187kJ.mol⁻¹) for the oxidation of chemisorbed carbon (**R4**) which would imply that this step is rather difficult. Hence, the catalyst will deactivate by coking while they did not present experimental evidence for such behavior. Also, some other authors reported positive values of standard adsorption enthalpy which rarely occur besides reporting standard adsorption entropies that are higher than the limit of thermodynamic consistency (–41.8J.mol⁻¹.K⁻¹).^{39,40} In some other instances, the models and their parameters were not subjected to statistical validation. All these aspects make these expressions inadequate for a robust reactor

modelling and design, where is desired a model that describes the catalytic sequence of the dry reforming of methane reaction with a physicochemical and statistical basis.^{41–43}

Table 1. Langmuir–Hinshelwood models for Ni–La₂O₃ catalysts. *MASI = Most Abundant Surface Intermediate.

MASI*		Rate expression	Reference
Ni	La ₂ O ₃		
C	CO ₂	$r_{\text{CH}_4} = \frac{K_{\text{CH}_4} k_2 K_{\text{CO}_2} k_4 p_{\text{CH}_4} p_{\text{CO}_2}}{K_{\text{CH}_4} k_2 K_{\text{CO}_2} p_{\text{CH}_4} p_{\text{CO}_2} + K_{\text{CH}_4} k_2 p_{\text{CH}_4} + K_{\text{CO}_2} k_4 p_{\text{CO}_2}}$ $K_{\text{CH}_4} k_2 = 2.61 \times 10^{-3} e^{-\frac{4300}{T}}$ $K_{\text{CO}_2} = 5.17 \times 10^{-5} e^{\frac{8700}{T}}$ $k_4 = 5.35 \times 10^{-1} e^{-\frac{7500}{T}}$	35
CH ₄ C	CO ₂	$r_{\text{CH}_4} = \frac{K_{\text{CH}_4} k_2 K_{\text{CO}_2} k_4 p_{\text{CH}_4} p_{\text{CO}_2}}{K_{\text{CH}_4} k_2 p_{\text{CH}_4} + K_{\text{CO}_2} k_4 p_{\text{CO}_2} + K_{\text{CH}_4} k_2 K_{\text{CO}_2} p_{\text{CH}_4} p_{\text{CO}_2} + K_{\text{CH}_4} K_{\text{CO}_2} k_4 p_{\text{CH}_4} p_{\text{CO}_2}}$ $K_{\text{CH}_4} = 1.41 \times 10^{-1}$ $k_2 = 2.23 \times 10^{-4}$ $K_{\text{CO}_2} = 1.60 \times 10^{-2}$ $k_4 = 1.32 \times 10^{-2}$	29
CH ₄ C		$r_{\text{CH}_4} = \frac{K_{\text{CH}_4} k_2 K_{\text{CO}_2} k_4 p_{\text{CH}_4} p_{\text{CO}_2}}{K_{\text{CH}_4} k_2 K_3 p_{\text{CH}_4} p_{\text{CO}_2} + K_{\text{CH}_4} k_2 p_{\text{CH}_4} + K_{\text{CO}_2} k_4 p_{\text{CO}_2}}$ $K_1 = 2.98 \times 10^2 e^{-\frac{7500}{T}}$ $k_2 = 1.23 \times 10^1 e^{-\frac{10200}{T}}$ $K_{\text{CO}_2} k_4 = 3.40 \times 10^{-2} e^{-\frac{7000}{T}}$	37,38

Where, r_{CH_4} (mol.g⁻¹.s⁻¹) is the net CH₄ rate, p_i (kPa) the partial pressure of *i*-th compound, K_{CH_4} (kPa⁻¹) and K_{CO_2} (kPa⁻¹) are the adsorption constants for CH₄ (**R1**) and CO₂ (**R3**), respectively, while k_2 (mol.g⁻¹.s⁻¹) and k_4 (mol.g⁻¹.s⁻¹) are the forward reaction constants for CH₄ dehydrogenation (**R2**) and oxidation of chemisorbed carbon (**R4**), respectively.

Considering the above, the objective of this work was to study the kinetics of the dry reforming of methane over a solid solution Ni–La oxide catalyst of proven stability.^{44–46} Particularly, seven kinetic models based on six plausible Langmuir–Hinshelwood reaction mechanisms were postulated and tested. These models considered that the catalytic cycles could occur over different types of active sites and that they could involve either a single

active site or a pair of active sites. Also, all the assessed kinetic models considered the influence of the reaction steps involved in the generation of water via the competing reverse water gas reaction over the kinetics of dry reforming. The results of the investigation led to conclude that the best kinetic model representing the dry reforming of methane stems from the consideration that the cleavage of the C–H bond from methane takes place over a metal–oxygen pair site instead of over a metal–metal site. The model also predicted that the dissociation of CO₂ can inhibit dry reforming under certain reaction conditions by decreasing the apparent activation energy for CH₄ activation. This behavior is related to the dynamics of competition between methane dry reforming and the reverse water gas shift reaction. Overall, the present study helps to build a more robust and profound comprehension of the behavior of solid solution Ni–La oxide catalysts and paves the way for the rigorous modeling and scale–up of methane dry reforming reactors.

2. Results and discussion

In this section, the results of the physicochemical characterization of the synthesized catalyst, which includes a short-term stability test are presented first. Afterwards, the effect of the operation conditions over the net rates of reactions is studied. Then, a description of the reaction mechanism and of the assumptions made in the formulation of the kinetic model that best represented the kinetic performance of the synthesized solid solution Ni–La oxide catalyst under dry reforming of methane conditions is shown.

The experimental methods used in this study are comprehensively described in the Supplementary information. In order to guarantee the absence of heat and mass gradients in the reactor, criteria to ensure negligible radial and axial dispersion effects, sufficiently small radial and axial temperature gradients, absence of interfacial and intraparticle mass and heat transfer limitations, and low-pressure drop across the catalytic bed were verified, as summarized in **Table S2**. The details of the performed calculations can be found in the Supplementary information, section C. Thus, all rate and selectivity data reported herein are assumed to reflect the intrinsic catalytic events of the dry reforming of the methane over solid solution Ni–La oxide catalysts.

2.1. Physicochemical properties of the catalyst

Concerning the crystallinity of the catalyst, the XRD pattern for the as-synthesized solid solution Ni–La oxide presented three phases (**Figure 2A**); namely, tetragonal La_2NiO_4 or so-called Ruddlesden–Popper phase (layered-type perovskites), hexagonal $\text{La}(\text{OH})_3$, and cubic NiO whose compositions were 55, 25 and 20wt%, respectively, as determined via semi-quantitative analysis. After the hydrogen reduction treatment made before each catalytic test, the observed phases were cubic Ni and hexagonal $\text{La}(\text{OH})_3$ with a composition

of 24 and 76wt%, respectively. According to the above phase compositions, the total concentrations of Ni were 3992 and 4098 $\mu\text{mol Ni.g}_{\text{cat}}^{-1}$ for the fresh and reduced samples of the catalysts, respectively. These concentrations agreed with the nominal concentration of nickel of the material: 4072 $\mu\text{mol Ni.g}_{\text{cat}}^{-1}$. Crystallite diameters for NiO in the fresh sample and Ni in the reduced sample were estimated to be 30 and 50nm, respectively, as from calculations done with the Scherrer equation (eq S2) using the XRD peaks at 2θ of 37.3° and 44.6°, which corresponds to the diffraction planes for NiO(111) and Ni(111), respectively.⁴⁷ The larger crystallite diameter for the Ni phase can be related to the fact that ~64mol% out of the total amount of Ni in the reduced sample was due to the reduction of the NiO phase present in the fresh catalyst. This also suggests that the increase in the crystallite size from NiO in the fresh sample to Ni upon reduction can be due to sintering.^{48,49}

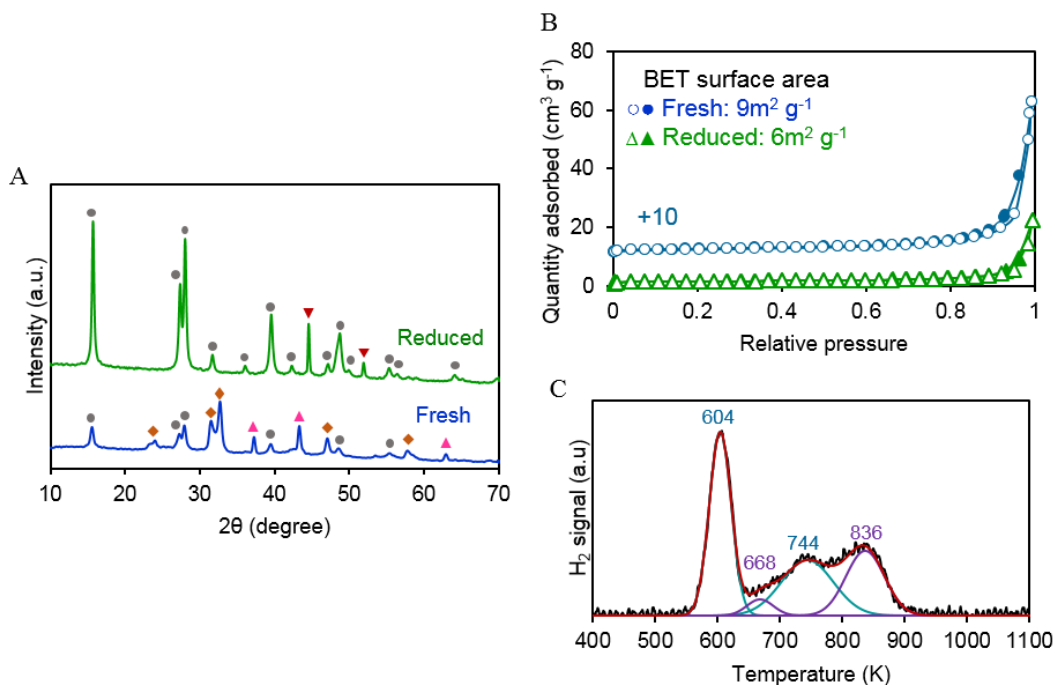


Figure 2. XRD pattern (A) and N_2 physisorption isotherms (B) of fresh (blue) and reduced sample (green, reduction under a H_2 space velocity of $1.7 \text{cm}^3 \text{g}^{-1} \text{s}^{-1}$ and 1023K for 1h with a heating rate of 0.083K s^{-1}) as well as the H_2 -TPR profile (C) of the fresh catalyst. XRD caption: Hexagonal $\text{La}(\text{OH})_3$ (\bullet), tetragonal La_2NiO_4 (\blacklozenge), cubic NiO (\blacktriangle) and cubic Ni (\blacktriangledown). N_2 physisorption caption: Adsorption ($\circ\triangle$) and desorption ($\bullet\blacktriangle$) branch.

On the other hand, the presence of $\text{La}(\text{OH})_3$ is likely because reduction was performed under pure H_2 . $\text{La}(\text{OH})_3$ is known to decompose to La_2O_3 and to a $\text{La}_2\text{O}_2\text{CO}_3$ phase under the presence of N_2 and CO_2 , respectively, at temperatures above 673K.^{50,51} Therefore, a Ni– $\text{La}_2\text{O}_2\text{CO}_3$ mixed phase should be present under the atmosphere of the dry reforming of methane process as demonstrated in previous works.^{17–19,25} However, no direct proof from the analysis of spent catalysts is presented herein because of the impossibility of recovering it after the catalytic tests considering the elevated bed dilution ratios (~99vol%) that were used to avoid temperature gradients in the catalytic bed.

The temperature programmed reduction profile of the fresh catalyst is shown in **Figure 2C**. The profile displayed four reduction peaks. The first peak, which consumed $1725\mu\text{mol H}_{2,\text{gcat}}^{-1}$, had its maximum at 604K and was assigned to the reduction of the nickel oxide phase into metallic nickel.^{48,49} The second peak with an uptake of $183\mu\text{mol H}_{2,\text{gcat}}^{-1}$ at 668K was ascribed to the reduction of non-stoichiometric oxygen (+ δ) in $\text{La}_2\text{NiO}_{4+\delta}$ to form La_2NiO_4 . Where, the value of δ was determined to be 0.17 from the corresponding H_2 uptake. The estimated value of δ was within the range reported for this kind of material.⁵² The third peak, which consumed $1229\mu\text{mol H}_{2,\text{gcat}}^{-1}$ at 744K, was associated with a second NiO reduction peak.^{48,49,53} According to the literature, this peak is due to the reduction of bulk NiO in larger oxide particles, where the nucleation rate of metallic Ni from the surface to the bulk NiO and the outward diffusion of water is low at reduction temperatures lower than 700K hence leading to mixtures between NiO–Ni.^{48,49,53} In this sense, the noncomplete reduction of NiO in the first peak at 604K yielded a NiO–Ni product whose composition, as determined from the H_2 uptakes, was 42 and 58mol% of NiO and Ni, respectively. After that, such mixture was reduced into metallic Ni in the third reduction step centered at 744K. Finally, the fourth peak with an uptake of $1076\mu\text{mol H}_{2,\text{gcat}}^{-1}$ and centered at 836K was

assigned to the reduction of La_2NiO_4 into Ni and La_2O_3 ($\text{La}_2\text{NiO}_4 + \text{H}_2 \rightleftharpoons \text{Ni} + \text{La}_2\text{O}_3 + \text{H}_2\text{O}$).^{54,55} According to the stoichiometry of the above reduction steps and H_2 uptakes, the total concentration of Ni in the sample was $4029\mu\text{mol Ni.g}_{\text{cat}}^{-1}$ from which 73mol% corresponds to NiO. Such values were close to those estimated by XRD hence indicating that the degree of reduction of the sample was about 100%.

Regarding the texture of the catalyst, N_2 physisorption results (**Figure 2B**) showed that both the fresh and the reduced catalyst presented IUPAC's Type II isotherms, which are characteristic of macroporous materials.⁵⁶ According to the calculations made from the physisorption data, the BET surface area decreased from $9\text{m}^2.\text{g}_{\text{cat}}^{-1}$ (BET constant or $C_{\text{BET}} = 770$) for the fresh catalyst to $6\text{m}^2.\text{g}_{\text{cat}}^{-1}$ ($C_{\text{BET}} = 500$) for the reduced catalyst. According to the literature, metal oxides synthesized via the citrate complexing method are composed of agglomerated semispherical-shaped particles, where the macropores result from interparticle voids.⁵⁷⁻⁵⁹ In this context, when the reduction process was performed, the particles of the catalyst sintered, which was evidenced from the XRD results, hence making fewer macropores.⁶⁰

Calculations from H_2 chemisorption data resulted in a concentration of $19\mu\text{mol Ni.g}_{\text{cat}}^{-1}$ at the surface of the catalyst. Accordingly, the dispersion of nickel was 0.46% and the mean particle diameter of nickel was 220nm (**eq S1**). Therefore, there was a four times difference between the mean crystallite and particle size estimated from the DRX and chemisorption methods, respectively. Such a large difference could either be because of the polycrystalline nature of the Ni particles⁶⁰ or because, for the type of catalyst studied herein, the Ni particles are typically encapsulated or incorporated into the oxide matrix of the Ni- La_2O_3 phase^{16,19,61}. For the latter scenario, only a tiny fraction of the reduced metal is exposed on the surface hence yielding such a low H_2 chemisorption capacity as the one determined

herein. Whatever the explanation for the differences found between the estimation of particle size from XRD and chemisorption may be, the fact remains that the latter is the most suitable metrics to be considered for interpreting the catalytic behavior.

Finally, to assess the stability of the catalyst under the conditions of the methane dry reforming reaction, two catalytic tests were performed by flowing reactants (CH_4 and CO_2) and both reactants and products (CO and H_2) at 873K for 10h. The results of these tests in terms of the net reaction rates of CH_4 and CO_2 with time on stream demonstrates that both in the absence, **Figure 3A**, and in the presence, **Figure 3B**, of products the net CH_4 rate showed a steady state value of $\sim 0.40 \text{ mol.kg}_{\text{cat}}^{-1}.\text{s}^{-1}$, while the net CO_2 rate displayed a steady state value of ~ 0.55 and $1.05 \text{ mol.kg}_{\text{cat}}^{-1}.\text{s}^{-1}$ in the absence and presence of products, respectively. Therefore, the catalyst did not show deactivation within the sampling space of the current study; a result that agrees with previous findings concerning the behavior of Ni– La_2O_3 catalysts synthesized by the solid–state decomposition of perovskite type precursors.^{17,23,29} Furthermore, this result also shows that the steps for CH_4 activation were not inhibited by the presence of reaction products. In contrast, the steps for the CO_2 activation were favored because, as explained below, the larger availability of H_2 in the reactor favors the conversion of this reactant via the RWGS reaction.

Ni– La_2O_3 based catalysts are usually synthesized via either the impregnation of nickel nitrate salts^{25,62,63} or the solid–state decomposition of the perovskites LaNiO_3 and La_2NiO_4 .^{54,64–68} The latter method can yield solid solution Ni–La oxide catalysts with mean Ni particle sizes lower than 30nm and BET surface areas lower than $20 \text{ m}^2.\text{g}_{\text{cat}}^{-1}$, depending on synthesis route of the parent perovskite, and stable after (very) long time on stream.^{44–46,54,64–68} Thus, although the catalyst precursor herein synthesized was composed of different phases, namely, NiO, La_2NiO_4 , and $\text{La}(\text{OH})_3$, its solid–state thermal decomposition yielded

a Ni(220nm average particle size)–La oxide catalyst with stability comparable to that of the materials obtained from pure perovskite phases.

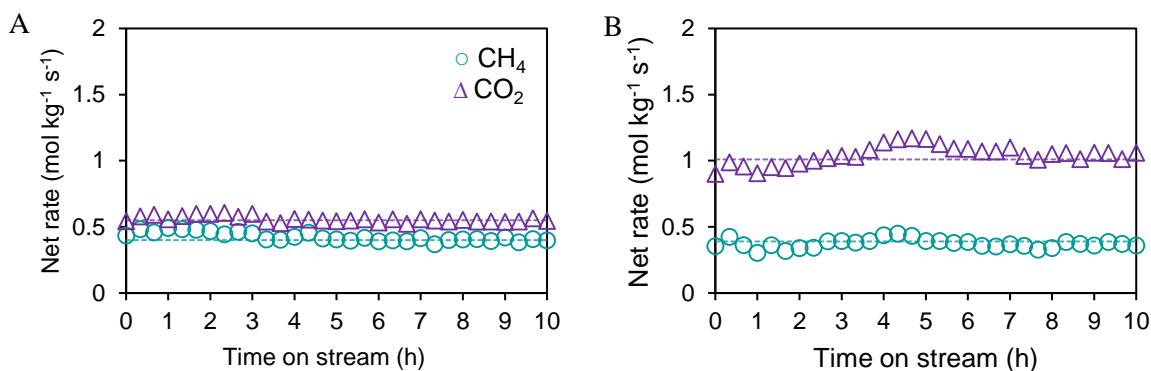


Figure 3. Catalyst activity in the absence (A) and in the presence (B) of H₂ and CO as a function of the time on stream (39.0kPa CH₄, 39.0kPa CO₂, 5.9kPa H₂ (B), 5.9kPa CO (B), balance N₂, 130kPa total pressure, and 873K).

2.2. Overall catalytic performance

First of all, an analysis to classify the reaction products as primary, secondary, or higher is presented using the so-called delplot analysis.⁶⁹ For the analysis, when either the selectivity or the selectivity/conversion ratio was plotted versus the conversion and the intercept at zero conversion gives information about primary or secondary products, respectively. The intercept at zero conversion can be evaluated via linear regression. Herein, correlation coefficients R² higher than 0.98 were always found (**Figure 4**, solid lines). **Figure 4** shows the first (**Figure 4A**) and second-rank (**Figure 4B**) delplot analysis plots for CH₄. Accordingly, among the three reaction products, H₂O, CO, and H₂, only water was determined to be a secondary product derived from methane because it showed a zero and a finite intercept of 6.9 ± 1.0 in the first- and second-rank plots, respectively. On the other hand, CO and H₂O were determined to be primary products from CO₂ with finite intercepts of 0.6 ± 0.1 and 0.2 ± 0.1 , respectively, in the first-rank plots, **Figure 4C**.

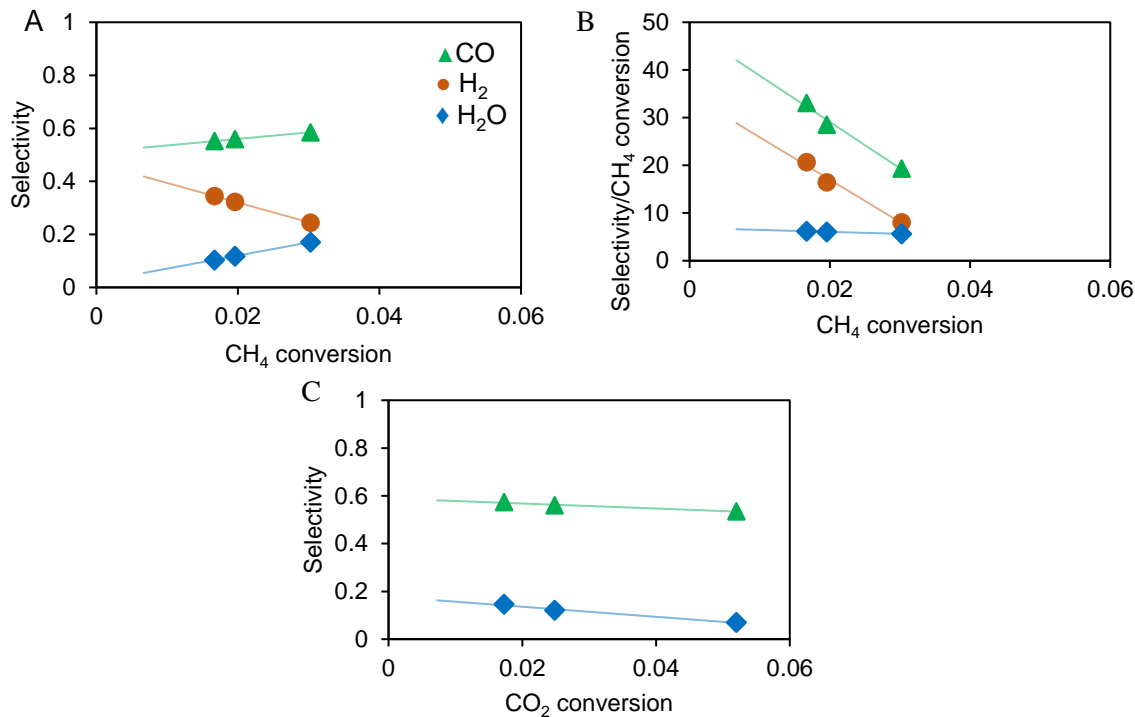


Figure 4. CH₄ (A) and CO₂ (C) first-rank as well as CH₄ second-rank (B) delplot analysis (39kPa of CO₂ (A and B) or CH₄ (C), N₂ balance, 130kPa total pressure, and 923K). Symbols represent experimental observations and solid lines were calculated via linear regression, correlation coefficients $R^2 > 0.98$.

The results of the delplot analysis agree with what is known about the occurrence of the reverse water gas shift reaction during dry reforming of methane over Ni-based catalysts. Particularly, experimental^{11,70–72} and molecular simulations^{36,73,74} studies have reported that the RWGS reaction can proceed through the interaction of chemisorbed hydrogen from the dehydrogenation of CH₄ and oxygen adatoms from the dissociation of CO₂ ($\text{CO}_2^* + * \rightleftharpoons \text{CO}^* + \text{O}^*$) to produce chemisorbed hydroxyl species ($\text{H}^* + \text{O}^* \rightleftharpoons \text{OH}^* + *$) that in turn would react with another hydrogen adatom to produce adsorbed water ($\text{H}^* + \text{OH}^* \rightleftharpoons \text{H}_2\text{O}^* + *$).

The influence of the explored reaction conditions, i.e., the sampling space, on the catalyst activity and product distribution is presented below. In general, within the investigated sampling space, the effects of the partial pressure of the reactants and products as well as the temperature over the net reaction rates did not show statistically significant

deviations from linearity; i.e., no quadratic and interaction effects (**eq S12**) were detected, see details in the Supplementary Information, Section B. For the following analyses, *t*-Student 95% confidence intervals were estimated for the grand media of the data, i.e., the media of all the performed experimental measurements, to provide a quick idea about which input variables have statistically relevant effects over the estimated reaction rates. In this sense, when the experimental values plotted in these graphs are found outside the estimated confidence interval for the grand media, the effect of the analyzed input variable over the response variable may be considered statistically significant. A similar method was proven to be of utility in previous works.⁷⁵

The effect of the partial pressures of the reactants over the net reaction rates is depicted in **Figure 5**. As observed, increasing the CH₄ pressure from 16.9 to 61.1kPa, **Figures 5A–C**, increased the net rates of CH₄, from 0.36 to 0.84mol.kg_{cat}⁻¹.s⁻¹, CO₂, from 0.57 to 0.98mol.kg_{cat}⁻¹.s⁻¹, CO, from 0.96 to 1.62mol.kg_{cat}⁻¹.s⁻¹, and H₂, from 0.40 to 1.01mol.kg_{cat}⁻¹.s⁻¹, significantly. In contrast, the net H₂O rate was kept constant at an average of 0.27 ± 0.05mol.kg_{cat}⁻¹.s⁻¹, **Figure 5C**. On the other hand, increasing the CO₂ pressure from 16.9 to 61.1kPa, **Figures 5D–F**, kept both the net rates of CO₂ and CO constant at an average of 0.75 ± 0.15mol.kg_{cat}⁻¹.s⁻¹ and 1.29 ± 0.28mol.kg_{cat}⁻¹.s⁻¹, respectively, while the net H₂O rate increased significantly, from 0.18 to 0.33mol.kg_{cat}⁻¹.s⁻¹ and the net H₂ rate decreased significantly, from 1.04 to 0.64mol.kg_{cat}⁻¹.s⁻¹, **Figure 5E**. On the other hand, the effect of the CO₂ pressure over the net CH₄ rate was negative, and the rate decreased from 0.66 to 0.47mol.kg_{cat}⁻¹.s⁻¹, *p*-value of 0.055, **Figure S2A**. In this case, one would say that the effect of this input variable was negative but weak.

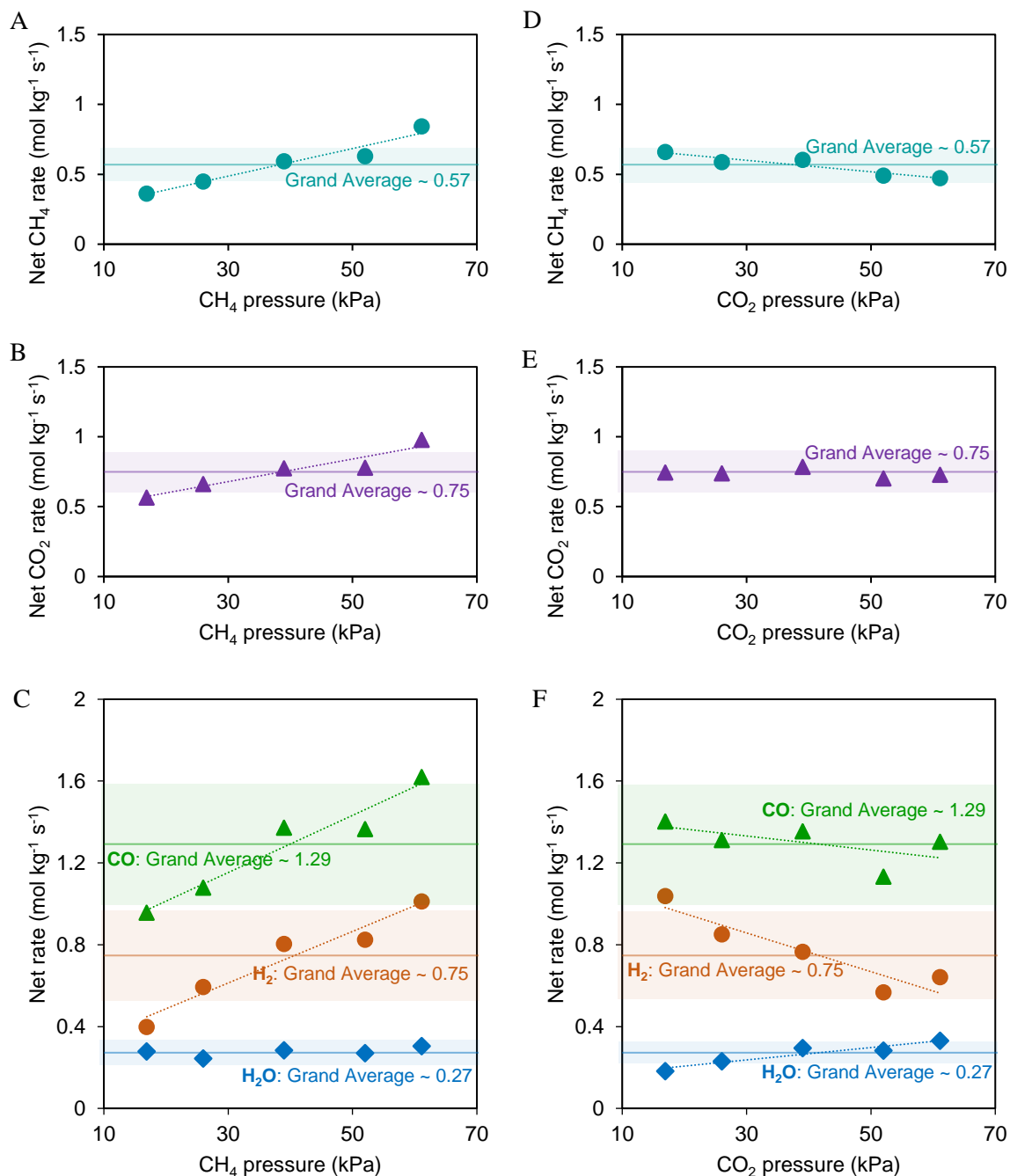


Figure 5. Main effect plots of the reactant pressure for the first set of experiments (conditions: 39kPa CH₄ (A–C) or CO₂ (D–F), balance N₂, 130kPa total pressure and 923K). Shaded areas correspond to *t*-Student confidence intervals for the mean built at a confidence level of 95%, with $n_{\text{exp}} - 1$ (i.e., 16) degrees of freedom.

The influence of feeding products on the reactor performance is shown in **Figure 6**.

In general, increasing the CO pressure from 0.3 to 11.4kPa, **Figures 6A–C**, did not affect any net rates. Therefore, one may conclude that all the reactions are zero-order with respect

to CO. Similarly, when the partial pressure of H₂ was increased, from 0.3 to 11.4kPa, **Figures 6D–F**, the net CH₄ rate did not change significantly hence indicating that there was not inhibition of the methane dry reforming reaction by this product. This can also be perceived by comparing the grand media for the net CH₄ rate in the two experimental sets: 0.57 and 0.62mol.kg_{cat}⁻¹.s⁻¹ for the first and second one, respectively. Therefore, it is safe to assume that the dry reforming reaction is zero–order with respect to both CO and H₂. On the other hand, such an increment in the H₂ pressure significantly increased the net rates of CO₂, from 0.91 to 1.85mol.kg_{cat}⁻¹.s⁻¹, CO, from 1.32 to 2.26mol.kg_{cat}⁻¹.s⁻¹, and H₂O, from 0.28 to 1.36mol.kg_{cat}⁻¹.s⁻¹, although the H₂ rate decreased significantly, from 0.76 to -0.46mol.kg_{cat}⁻¹.s⁻¹, **Figure 6F**. These trends were also observed when the two experimental sets were contrasted; specifically, there was an increment from the first to the second set in the grand media of the net rates of CO₂, from 0.75 to 1.47mol.kg_{cat}⁻¹.s⁻¹, CO, from 1.29 to 2.05mol.kg_{cat}⁻¹.s⁻¹, and H₂O, from 0.27 to 0.94mol.kg_{cat}⁻¹.s⁻¹, while the net H₂ rate was reduced from 0.75 to 0.17mol.kg_{cat}⁻¹.s⁻¹. In this instance, the negative values of the net H₂ rates are due to a higher conversion rate of the product in the RWGS reaction in front of its production rate from the dry reforming of methane reaction. For example, the stoichiometric relationship between the dry reforming of methane and RWGS reaction, as determined with the CH₄/H₂O ratio of the net rates, is 0.40 at 9.1kPa H₂ that, in other words, indicates 0.8mol H₂ produced in the dry reforming per 1mol H₂ converted in the RWGS reaction, so leading to the additional requirements of H₂.

It is well–known that products can inhibit catalytic reaction rates because of competitive adsorption over the free active sites of the catalyst and because of an increase of the reverse reaction rate of the steps involved in the product formation given its higher surface

concentration. Taking this into account, the current results suggest that the CO coverage is low enough to avoid the inhibition of the dry reforming and RWGS reactions.

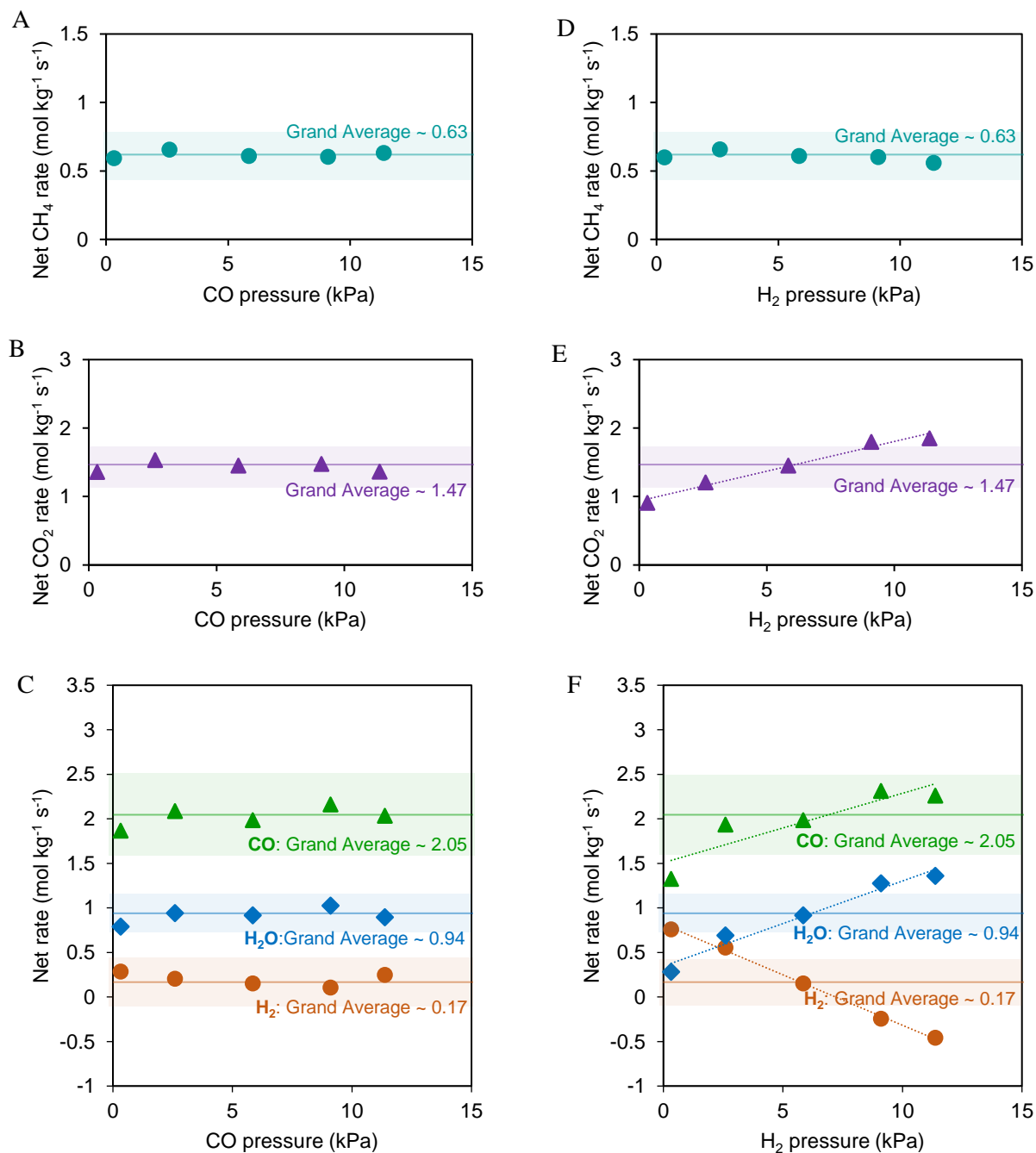


Figure 6. Main effect plots of product pressure for the second experimental set (conditions: 5.9kPa H₂ (A–C) or CO (D–F), 39kPa CH₄, 39kPa CO₂, balance N₂, 130kPa total pressure, and 923K). Shaded areas correspond to *t*-Student confidence intervals for the mean built at a confidence level of 95%, with $n_{\text{exp}} - 1$ (i.e., 16) degrees of freedom.

In the literature, the CH₄ conversion rate was reported to be independent of the partial pressure of CO₂, CO, and H₂ over the partial pressure range of 5–400kPa for supported Ni(10nm)/MgO⁷¹, Ni(26nm)/MgO–ZrO₂¹¹ and Ni(30nm)/La₂O₃³⁵ catalysts. Herein, we found evidence, supported by statistics, that the CO₂ affected weakly the net CH₄ rate while the CO and H₂ did not influence it. It has been reported that nonconfined Ni clusters on the support are more susceptible to oxygen deactivation by promoting the CO₂ dissociation than those embedded in the oxide.⁷⁶ In this sense, the discrepancy with the cited reports that discarded the effect of the CO₂ over the CH₄ conversion rate could be caused by the difference in Ni particle size and, in turn, by the metal–support interactions. Indeed, transmission electron microscopy analysis revealed that for spent solid solution Ni–La₂O₃ catalysts (923–1073K, space velocity = 3–35cm³.g⁻¹.s⁻¹, 10–20kPa for both CH₄ and CO₂) with a mean metal size of 10–30nm there was a continuous layer of La₂O₂CO₃ covering the Ni particles.^{17,23} However, such a layer may not exist for the large Ni particles of the solid solution Ni–La oxide catalyst studied herein.

To further explore the above hypothesis, a thermodynamic analysis of the chemical state of the Ni particles in the synthesized solid solution Ni–La oxide catalyst under the operational conditions was done. The analysis was made considering the free reaction energy required for the formation of bulk NiO with CO₂ (Ni + CO₂ ⇌ NiO + CO) that is related to the CO₂/CO pressure ratio in the reactor according to the following equation:

$$\Delta G^0 = RT \ln \left(\frac{a_{\text{Ni}} p_{\text{CO}_2}}{a_{\text{NiO}} p_{\text{CO}}} \right) \quad (1)$$

Where, a_{Ni} and a_{NiO} refer to the thermodynamic activity of solid Ni and NiO, whose values are the unity for pure phases.¹¹ According to calculations, the free energy ranges from 47 to 48kJ.mol⁻¹ under the temperatures (838–1008K) tested herein. With which, the CO₂/CO

pressure ratio required for the formation of bulk NiO is between 270–945, which are values significantly higher than those used in the present tests: 2–70. Thus, the bulk Ni atoms belonging to the solid solution Ni–La oxide catalyst should remain in a metallic state while the metal surface atoms should be oxidized under the current reaction conditions. In this sense, it is likely that the net CH₄ rate decreases because of an increment in the oxygen coverage when the CO₂ pressure increase. This behavior was also observed for a Ni–Co(26nm)/MgO–ZrO₂ catalyst, where the incorporation of cobalt increased the cluster oxophilicity leading to a nearly saturated metal surface with chemisorbed oxygen adatoms derived from the CO₂ dissociation.¹¹ In such a report, it was shown that an increase of the CO₂ pressure from 5 to 30kPa with 20kPa CH₄ at 873K decreased the forward turnover of CH₄ rate from about 14 to 7s⁻¹. In our case, the increase of the CO₂ pressure from 26 to 52kPa with 26kPa CH₄ at 873K decreased the forward turnover CH₄ rate (**eq S6**) from 15 to 11s⁻¹, i.e., the current solid solution Ni–La oxide catalyst would be less sensitive to an increment of CO₂ pressure in comparison to the Ni–Co/MgO–ZrO₂, hence agreeing with the fact that Ni would be less oxophilic in these systems than in a Ni–Co alloy.¹¹

To summarize, the kinetic measurements showed that the dry reforming of methane reaction (or net CH₄ rate) was (1) promoted by increasing the CH₄ pressure, (2) weakly suppressed by the increment in the CO₂ pressure, and (3) unaffected by the CO and H₂ pressure. Such behavior suggests that the chemisorbed oxygen adatoms are a key intermediate in the catalytic sequence of dry reforming of methane over solid solution Ni–La oxide catalysts. The following section is devoted to further exploring this hypothesis.

2.3. Kinetic analysis of the results

2.3.1. Postulation of reaction mechanisms and kinetic models

Six different Langmuir–Hinshelwood reaction mechanisms and seven kinetic models were proposed to analyze the kinetics of methane dry reforming over the synthesized solid solution Ni–La oxide catalyst. These mechanisms were based on both the data collected herein and on the extensive literature on this topic.^{4,5,10,11,17,19,25,35,36,71,73,74,76–80} In this section, the kinetics of the process is analyzed under the light of the model that best fitted the experimental data and fulfilled the thermodynamic consistency criteria, **Table 2**. The competing models are comprehensively explained in the Supplementary Information, section E, and summarized in **Table S8**.

Table 2. Dry reforming and RWGS reaction steps with corresponding stoichiometric numbers.

Step	Elementary step	Dry reforming	RWGS	Kinetic descriptor
1	$\text{CH}_4 + \text{O}^* + * \rightleftharpoons \text{CH}_3^* + \text{OH}^*$	1		k_1, K_1
2	$\text{CH}_3^* + * \rightleftharpoons \text{CH}_2^* + \text{H}^*$	1		k_2, K_2
3	$\text{CH}_2^* + * \rightleftharpoons \text{CH}^* + \text{H}^*$	1		k_3, K_3
4	$\text{CH}^* + * \rightleftharpoons \text{C}^* + \text{H}^*$	1		k_4, K_4
5	$\text{CO}_2^* + * \rightleftharpoons \text{CO}^* + \text{O}^*$	1	1	k_5, K_5
6	$\text{C}^* + \text{O}^* \rightleftharpoons \text{CO}^* + *$	1		k_6, K_6
7	$\text{H}^* + \text{O}^* \rightleftharpoons \text{OH}^* + *$	-1	1	k_7, K_7
8	$\text{OH}^* + \text{H}^* \rightleftharpoons \text{H}_2\text{O}^* + *$		1	k_8, K_8
9	$\text{CO}_2 + * \rightleftharpoons \text{CO}_2^*$	1	1	K_{CO_2}
10	$\text{H}_2 + * + * \rightleftharpoons \text{H}^* + \text{H}^*$	-2	1	K_{H}
11	$\text{CO} + * \rightleftharpoons \text{CO}^*$	-2	-1	K_{CO}
12	$\text{H}_2\text{O} + * \rightleftharpoons \text{H}_2\text{O}^*$		-1	$K_{\text{H}_2\text{O}}$
Global reaction				
A	$\text{CH}_4 + \text{CO}_2 \rightleftharpoons 2\text{CO} + 2\text{H}_2$	1		
B	$\text{CO}_2 + \text{H}_2 \rightleftharpoons \text{CO} + \text{H}_2\text{O}$		1	

Key to symbols: *, an unoccupied metal site; #, an unoccupied oxide site; \rightleftharpoons , a quasi-equilibrated step; and \rightleftharpoons , a reversible step; k_n and K_n are the forward reaction rate constant and the reaction equilibrium coefficient of the n-th elementary reaction step

The selected model was based on a reaction mechanism that considered a single-site mechanism in which both CO₂ and CH₄ are activated over Ni-sites (symbolized by *). Specifically, it considers that the first C–H bond cleavage on methane takes place over a metal–oxygen pair site (*–O*, step 1), which is followed by a cascade of C–H cleavage steps until chemisorbed C adatoms (step 2–4). In parallel to this, CO₂ is adsorbed (step 9) and dissociated into chemisorbed CO and O (step 5); afterwards, the interaction between chemisorbed C and O adatoms produces another molecule of CO (step 6). Finally, the interaction of chemisorbed H and O adatoms produce OH species (step 7) which react with another H adatom to yield water (step 8).

The CO₂, CO, H₂, and H₂O (i–th species) adsorption steps were assumed to be quasi-equilibrated (**eq 2**). Specifically, dissociative adsorption of H₂ on Ni-sites were considered (**eq 3**). All the adsorbed reactants and product as well as the reaction intermediates; namely, CH₃, CH₂, CH, C, O and OH (j–th species), were accounted for the metal site balances (**eq 4**):

$$[i^*] = K_i \frac{p_i}{p^0} [*] \quad (2)$$

$$[H^*] = \sqrt{K_H \frac{p_{H_2}}{p^0}} [*] \quad (3)$$

$$[*]_{\text{tot}} = \sum[i^*] + \sum[j^*] + [*] \quad (4)$$

Where, p_i is the partial pressure of the i–th species, p^0 the standard pressure (1bar or 100kPa), $[i^*]$ is the surface concentration of i–th specie over a Ni-site, $[*]$ is the concentration of unoccupied metal sites and $[*]_{\text{tot}}$ is the total concentration of active sites that were determined to be $19\mu\text{mol Ni.g}_{\text{cat}}^{-1}$ from H₂ chemisorption. The reaction rate constant for the

reverse reactions (k_n^r) was expressed by the forward reaction rate constant (k_n^f) and the reaction equilibrium coefficient (K_n):

$$k_n^r = \frac{k_n^f}{K_n} = \frac{k_n}{K_n} \quad (5)$$

The pseudo-steady state approximation was applied to the concentration of the intermediates (j-th species), i.e., their net production rate was set equal to zero.^{81,82} With this, the following system of differential-algebraic equations (or DAE) was obtained:

$$\frac{dF_{CH_4}}{dw} = -k_1 \frac{p_{CH_4}}{p^0} [O^*][*] + \frac{k_1}{K_1} [CH_3^*][OH^*] \quad (6)$$

$$\frac{dF_{CO_2}}{dw} = -k_5 [CO_2^*][*] + \frac{k_5}{K_5} [CO^*][O^*] \quad (7)$$

$$\frac{dF_{CO}}{dw} = k_5 [CO_2^*][*] - \frac{k_5}{K_5} [CO^*][O^*] + k_6 [C^*][O^*] - \frac{k_6}{K_6} [CO^*][*] \quad (8)$$

$$2 \frac{dF_{H_2}}{dw} = k_2 [CH_3^*][*] - \frac{k_2}{K_2} [CH_2^*][H^*] + k_3 [CH_2^*][*] - \frac{k_3}{K_3} [CH^*][H^*] + k_4 [CH^*][*] \quad (9)$$

$$- \frac{k_4}{K_4} [C^*][H^*] - k_7 [H^*][O^*] + \frac{k_7}{K_7} [OH^*][*] - k_8 [OH^*][H^*] + \frac{k_8}{K_8} [H_2O^*][*]$$

$$\frac{dF_{H_2O}}{dw} = k_8 [OH^*][H^*] - \frac{k_8}{K_8} [H_2O^*][*] \quad (10)$$

$$k_1 \frac{p_{CH_4}}{p^0} [O^*][*] - \frac{k_1}{K_1} [CH_3^*][OH^*] - k_2 [CH_3^*][*] + \frac{k_2}{K_2} [CH_2^*][H^*] = 0 \quad (11)$$

$$k_2 [CH_3^*][*] - \frac{k_2}{K_2} [CH_2^*][H^*] - k_3 [CH_2^*][*] + \frac{k_3}{K_3} [CH^*][H^*] = 0 \quad (12)$$

$$k_3 [CH_2^*][*] - \frac{k_3}{K_3} [CH^*][H^*] - k_4 [CH^*][*] + \frac{k_4}{K_4} [C^*][H^*] = 0 \quad (13)$$

$$k_4 [CH^*][*] - \frac{k_4}{K_4} [C^*][H^*] - k_6 [C^*][O^*] + \frac{k_6}{K_6} [CO^*][*] = 0 \quad (14)$$

$$-k_1 \frac{p_{CH_4}}{p^0} [O^*][*] + \frac{k_1}{K_1} [CH_3^*][OH^*] + k_5 [CO_2^*][*] - \frac{k_5}{K_5} [CO^*][O^*] - k_6 [C^*][O^*] \quad (15)$$

$$+ \frac{k_6}{K_6} [CO^*][*] - k_7 [H^*][O^*] + \frac{k_7}{K_7} [OH^*][*] = 0$$

$$\begin{aligned}
& k_1 \frac{P_{\text{CH}_4}}{p^0} [\text{O}^*][*] - \frac{k_1}{K_1} [\text{CH}_3^*][\text{OH}^*] + k_7 [\text{H}^*][\text{O}^*] - \frac{k_7}{K_7} [\text{OH}^*][*] - k_8 [\text{OH}^*][\text{H}^*] \\
& + \frac{k_8}{K_8} [\text{H}_2\text{O}^*][*] = 0
\end{aligned} \tag{16}$$

Where, the number two on the left term in **eq 9** corresponds to the stoichiometric coefficient in the dissociative H₂ adsorption (step 10 in **Table 2**) since the right term corresponds to the net H species rate, i.e., 2 r_{H₂} = r_{H*}. The temperature dependence of the rate and equilibrium coefficients were expressed by the Arrhenius (**eq 17**) and van't Hoff (**eq 18**) equations, respectively:

$$k_n = A_n e^{-\frac{E_{a,n}}{RT}} \tag{17}$$

$$K_n = e^{\frac{\Delta S_n^0}{R}} e^{-\frac{\Delta H_n^0}{RT}} \tag{18}$$

Where, for the n–th reaction, A_n is the pre–exponential factor, E_{a,n} the activation energy, ΔS_n⁰ the standard reaction or adsorption entropy, ΔH_n⁰ the standard reaction or adsorption enthalpy, T the reaction temperature, and R the universal gas constant. As it can be noted, this model accounted for eight rate coefficients, eight surface reaction equilibrium coefficients, and four adsorption coefficients, with which the total number of kinetic parameters to be estimated equals forty. To reduce the number of the parameters to be estimated during the solution of the system of equations, the transition state theory (or TST) together with statistical thermodynamics was used to determinate the pre–exponential factors as well as the standard reaction and adsorption entropies of the model. This is explained in detail in the Supplementary Information, section D. These parameters were kept fixed during the regression of models, with which the number of adjustable parameters was halved.

2.3.2. Analysis of the solution of the kinetic models

The estimates for activation energies and standard surface reaction, and adsorption enthalpies obtained from the weighted regression of the best kinetic model are presented in **Table 3**. **Table S9** shows these estimates for the competing models. The agreement between the experimental and calculated net rates with corresponding F -values and BIC is depicted in **Figure 7**. As observed, the model showed an F -value for the global significance of the regression that exceeded the tabulated F -value of 2.79. Furthermore, all parameters were estimated statistically significant with t -values ranging from 30 to 300, which are larger than the tabulated t -value of 1.96, as well as with very narrow confidence intervals. This model was the one that best described the experimental net rates, as it can be noted by comparing its parity diagram in **Figure 7** to that of the other models in **Figure S5**, and displayed the highest F -value and lowest BIC (eq S46), which implies the best fitting of the data.

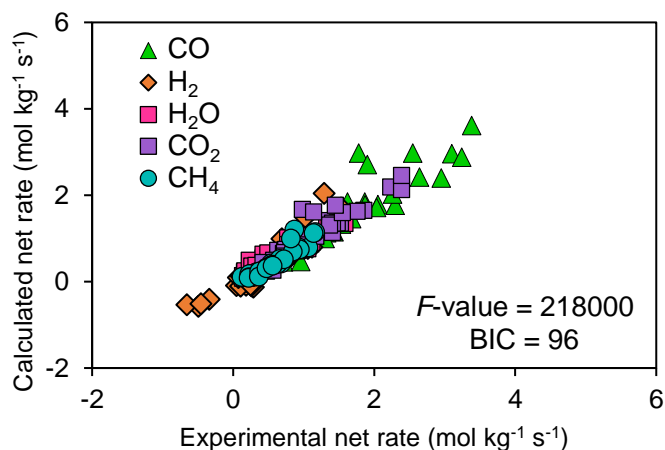


Figure 7. Parity diagram for comparing the experimental and calculated net rates of reactants conversion and products formation.

The physicochemical analysis of the kinetic and adsorption parameters showed that all adsorption enthalpies and entropies presented thermodynamic consistency (eq S41–S45) and both forward and reverse activation energies ($\Delta H_n^0 = E_{a,n}^f - E_{a,n}^r$) in the model were

within the range of thermodynamic consistency proposed by Santacesaria⁸³, which goes from 21 to 210kJ.mol⁻¹. Moreover, the calculated dry reforming and RWGS overall standard reaction entropies for the developed model were equal to 286 and 32J.mol⁻¹.K⁻¹, respectively, and they agreed with the experimental data; namely, 284.5 and 33.0J.mol⁻¹.K⁻¹ at 923K for the dry reforming and the RWGS reactions, respectively.⁸⁴ Similarly, the model displayed an overall dry reforming and RWGS standard reaction enthalpy of 260 ± 2 and 35 ± 1kJ.mol⁻¹, respectively, which is consistent with the experimental data, namely: 260.3 and 35.8kJ.mol⁻¹ at 923K for the dry reforming and the RWGS reactions, respectively.⁸⁴

In general, the estimated pre-exponential factors (**eq S50**) were identical to those reported by Dumesic et al.⁸⁵ and estimated with the methodology proposed by Campbell et al.⁸⁶, **Table 3**. Similarly, the activation energies, as well as the standard reaction and adsorption enthalpies in this model, matched those reported in microkinetic modelling studies,^{41,74,80} molecular simulations over Ni surfaces,^{36,73,76,77,87,88} and experimental data.^{11,71} For example, the activation energy for the oxygen-assisted C–H bond cleavage (step 1, **Table 2**) was in close agreement with the experimental value of 95kJ.mol⁻¹ for Ni–Co catalyst¹¹ and microkinetic studies of 88–93kJ.mol⁻¹ for Ni–based catalysts.^{74,80} Likewise, the reaction enthalpy for this step matched with the value of –8.0kJ mol⁻¹ reported elsewhere.⁸⁷ The values of the activation energy and reaction enthalpy for the sequential H–abstraction reactions (step 2–4) were in the range of 65–130kJ.mol⁻¹,^{36,41,73,74,80} and even their trend, i.e., a decrease in the activation energy upon the first H–abstraction and increase again for the last H–scission was similar to those predicted with molecular simulations.^{36,73,76,88} Moreover, the steps involved in H₂O production (steps 7 and 8) displayed activation energies of 89 ± 3 and 48 ± 3kJ.mol⁻¹, respectively, which were close to the values of 104 and 41kJ.mol⁻¹ reported in microkinetic models.^{74,80} Also, the corresponding standard enthalpies of 28 ± 1

and $-27 \pm 1 \text{ kJ.mol}^{-1}$ were in the reported range from 18 to 74 kJ.mol^{-1} and -52 to 41 kJ.mol^{-1} , respectively.^{36,41,73,74,80} Finally, the current model presented energy barriers for the CO_2 dissociation (step 5) and carbon oxidation (step 6) of 66 ± 2 and $-95 \pm 5 \text{ kJ.mol}^{-1}$, respectively, that agreed with the ranges reported in the literature and that goes from 65 – 89 kJ.mol^{-1} and 54 – 153 kJ.mol^{-1} , respectively.^{36,73,74,76,80,88}

Table 3. Kinetic parameters with their *t*-Student confidence intervals built at a 95% confidence level.

Kinetic descriptor	A_n ($\text{kg.mol}^{-1}.\text{s}^{-1}$)	$E_{a,n}$ (kJ.mol^{-1})	ΔS_n^0 ($\text{J.mol}^{-1}.\text{K}^{-1}$)	ΔH_n^0 (kJ.mol^{-1})
k_1, K_1	1.4×10^9	93 ± 1	-41	-10 ± 1
k_2, K_2	7.1×10^{13}	90 ± 3	34	63 ± 2
k_3, K_3	6.1×10^{13}	83 ± 3	49	57 ± 2
k_4, K_4	3.1×10^{15}	90 ± 3	12	-28 ± 1
k_5, K_5	1.2×10^{13} (3×10^{14}) ^a	66 ± 2	34	-53 ± 1
k_6, K_6	2.8×10^{13} (8×10^{13}) ^a	95 ± 5	-2	-37 ± 2
k_7, K_7	7.4×10^{13}	89 ± 3	2	28 ± 1
k_8, K_8	4.1×10^{11} (2×10^{11}) ^a	48 ± 3	-53	-27 ± 1
K_{CO_2}			-89	-13 ± 1
K_{H}			-51	-65 ± 1
K_{CO}			-94	-89 ± 3
$K_{\text{H}_2\text{O}}$			-96	-76 ± 2
DRM			286	260 ± 2
RWGS			32	35 ± 1

Pre-exponential factors for LH reactions according to Dumesic et al.⁸⁵: $10^{11} \text{ kg.mol}^{-1}.\text{s}^{-1}$ for mobile transition state with rotation; $10^{13} \text{ kg.mol}^{-1}.\text{s}^{-1}$ for mobile transition state without rotation; and $10^{15} \text{ kg.mol}^{-1}.\text{s}^{-1}$ for immobile transition state without rotation.

^a Pre-exponential factor estimated with the methodology proposed by Campbell et al.⁸⁶

2.3.3. Coverage and degree of rate control analysis

Surface coverages ($\theta_i = [i^*]/[i^*]_{\text{tot}}$) for the intermediates CO, H, O, OH, and free Ni-sites are depicted in **Figure 8**. The coverages predicted for CO_2 , H_2O , and CH_x were lower than 0.001 so they were excluded from the analysis. It can be observed that by increasing the CH_4 pressure from 16.9 to 61.1 kPa (**Figure 8A**, solid lines), the CO, H adatoms, OH and free sites coverages increased 1, 6%, 1% and 10%, respectively, while the O atoms coverage

decreased 18%, respectively. However, raising the CO₂ pressure by the same magnitude as the one for CH₄ (**Figure 8B**, dashed lines) led to the opposite behavior with similar values, except for OH coverage that stayed constant at 0.01. These trends show that an excess and a reduction of the oxygen adatoms over the surface, respectively, may either hinder or promote the net rates of CH₄, CO, and H₂.

Once the products are co-fed (**Figure 8B**), the grand media for the oxygen coverage decreased 21%, while for H, free sites and OH coverages increased 12%, 6%, and 1%, respectively. Particularly, raising the H₂ pressure from 0.3 to 11.4kPa (**Figure 8B**, solid lines) increased the OH, H, and free sites coverages 1%, 19%, and 8%, respectively, which caused the promotion in the RWGS reaction as observed experimentally. Even though the oxygen coverage decreased, it remained as the most abundant surface intermediate. Thus, the mechanism of CH₄ activation was unaffected. Of course, an increase of the H₂ partial pressure above 11.4kPa should lead to a reduction in the O coverage enough to shift the C–H bond cleavage from occurring on a metal–oxygen pair site (*–O*) to a metal–metal pair site (*–*). This, together with the larger increase in free site coverage than that of OH, may explain why raising the H₂ pressure did not inhibit the net rate of CH₄ within the sample space considered herein.

On the other hand, rising the CO partial pressure from 0.3 to 11.4kPa (**Figure 8B**, dashed lines) led to an increase in the CO and free site coverages of 4% and 1%, respectively. In comparison, the O coverage decreased 5%, suggesting a promotion of the CO oxidation into CO₂, thus inhibiting the net CO₂ rate. However, it was estimated that the reduction in the calculated net CO₂ rate was only 8% and statistically insignificant in the range of CO pressure studied (0.3–11.4kPa). Similarly, the low CO coverage as well as these small

variations in the surface state caused by its pressure increase, did not affect the net CH₄ rate, as said earlier.

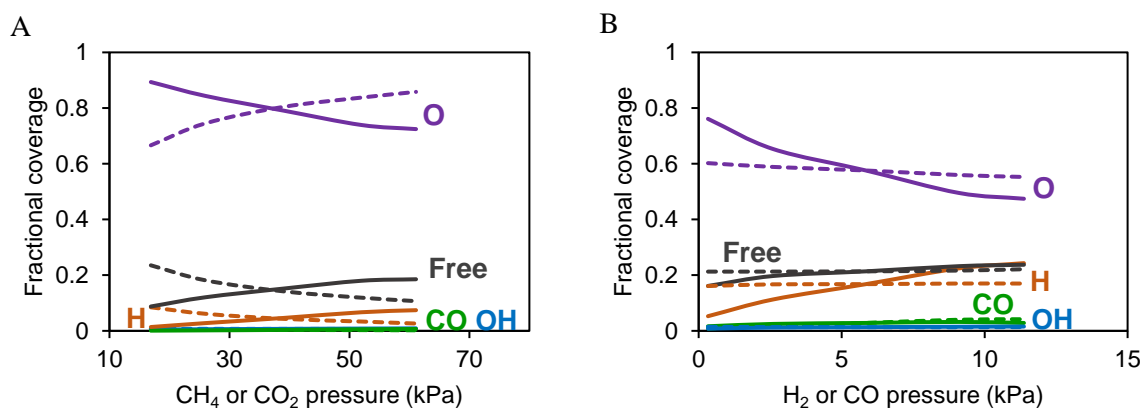


Figure 8. Calculated Ni surface coverage plotted versus reactants (A) and products (B) partial pressure. Dashed lines indicate the effect of the CO₂ (A) and CO (B) pressure. (conditions: 39.0kPa CH₄, 39.0kPa CO₂, 5.9kPa H₂ (B), 5.9kPa CO (B), balance N₂, 130kPa total pressure and 873K).

Figure 9 depicts the degree of rate control (eq S47) analysis at different operational conditions. It was found that only two steps out of the twelve considered in the mechanism presented non-zero X_{RC} values; namely, the oxygen-assisted CH₄ activation step, step 1 in **Table 2**, and the CO₂ dissociation step, step 5. The degree of rate control values of the steps changed markedly in both the presence and absence of H₂ and CO, as observed in **Figure 9**. It was found that the C–H bond activation step presented a DRC value of 1.37 at 39.0kPa of both CH₄ and CO₂ and 923K, which was reduced to 1.00 once 5.9kPa of both H₂ and CO were co-fed. Also, at such conditions, the CO₂ dissociation steps showed a degree of rate control value of –0.40 in the absence of products, which changed to zero in the presence of products. Therefore, the oxygen-assisted C–H cleavage was the rate-determining step (or RDS) under all experimental conditions in agreement with that reported for Ni^{11,71} and Pt^{70,72} clusters, while the CO₂ dissociation was an inhibition step (i.e., $X_{RC} < 0$) for the dry reforming reaction that became irrelevant by co-feeding products. As observed, raising the CO₂ partial

pressure from 16.9 to 61.1kPa (**Figure 9A**, dashed lines) increased the inhibition degree of the CO₂ dissociation by 22% and the degree of rate control value for the CH₄ activation step by 30%. Such a trend is explained by the increment in oxygen coverage that nearly saturates the nickel active sites (**Figure 8A**). On the other hand, increasing the CH₄ partial pressure (**Figure 9A**, solid lines) led to the opposite behavior, a decrease of 22% in the inhibition effect of the CO₂ dissociation while the degree of rate control value for CH₄ activation was reduced at the same proportion towards the unity as it corresponds to a reaction determining step. This was due to the fact that a raise of the CH₄ pressure reduced oxygen coverage (**Figure 8A**) at the same time that it increased that of the free sites leading to an adequate metal–oxygen (*–O*) pair site balance, thus reducing the inhibition effect caused by the excess of chemisorbed O adatoms. Indeed, increasing the H₂ pressure from 0.3 to 5.9kPa (**Figure 9B**, D; solid lines) made the CO₂ dissociation step irrelevant, while the DRC for CH₄ activation step reached unity. The change in the CO₂ dissociation step from inhibiting to irrelevant after co–feeding products directly affected the CH₄ apparent activation energy (eq S49) that is representative for dry reforming. Indeed, the CH₄ apparent activation energy increased from 65 ± 10 to $91 \pm 10\text{kJ}\cdot\text{mol}^{-1}$ when products were co–fed. On the other hand, increasing the CO pressure did not change the degree of rate control values (**Figure 9B**, dashed lines).

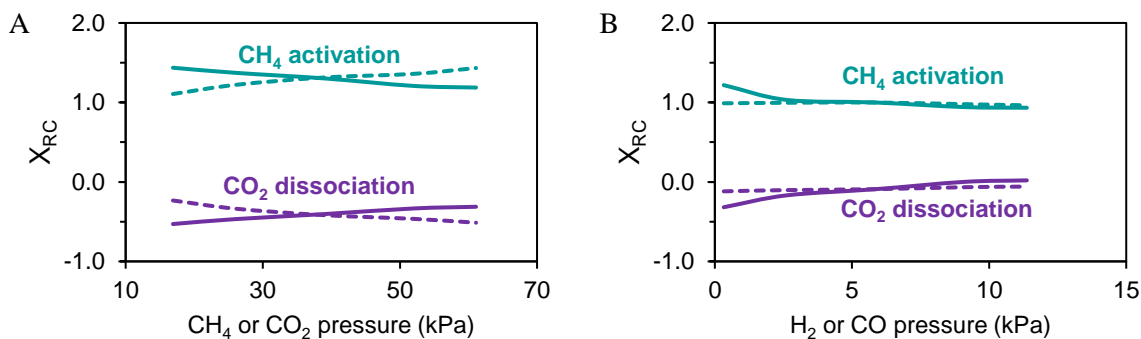


Figure 9. Calculated DRC of the oxygen–assisted CH₄ activation and CO₂ dissociation. Dashed lines indicate the effect of the CO₂ (A) and CO (B) pressure. (conditions: 39.0kPa CH₄, 39.0kPa CO₂, 5.9kPa H₂ (B), 5.9kPa CO (B), balance N₂, 130kPa total pressure and 873K).

Finally, the changes in apparent activation energy when a reaction is carried out in the presence of reaction products was recently discussed by Harris et al.⁸⁹, who found that the apparent activation energy of the NO oxidation ($\text{NO} + \frac{1}{2} \text{O}_2 \rightleftharpoons \text{NO}_2$) over a Cu–based catalyst increased from 22 to 45kJ.mol⁻¹ when NO₂ was co–fed with the reactants. The authors reported that NO₂ inhibited the forward rate and demonstrated that this unaccounted NO₂ inhibition effect, in reactions performed without products in the input stream, breaks the differential reactor approximation (or CSTR) and leads to errors in the measured kinetic parameter. However, in this case, the inhibition of CO and H₂ were not significant (i.e., zero–order). In order to explain this trend, let us rearrange **eq S47** by taking the partial derivative with respect to the temperature on both sides of the division term and by using the concept stated in **eq S49** which leads to **eq 19**. This expression shows that the contribution of the n–th elementary step to the apparent activation (termed as $[E_i^{\text{app}}]_n$) of the net rate of i–th compound is its activation energy ($E_{a,n}$) weighted by its degree of rate control:

$$X_{\text{RCi},n} = \frac{\frac{\partial \ln r_i}{\partial T}}{\frac{\partial \ln k_n}{\partial T}} = \frac{[E_i^{\text{app}}]_n}{E_{a,n}} \implies [E_i^{\text{app}}]_n = X_{\text{RCi},n} E_{a,n} \quad (19)$$

This expression is a generalized form of that reported by Jørgensen & Grönbeck⁹⁰ and Mao & Campbell⁹¹. In this way, as mentioned above, the grand average for the DRC value of the CO₂ dissociation step on the dry reforming was –0.4 that change to zero in the presence of a product, the former value together with its activation energy of $66 \pm 2\text{kJ.mol}^{-1}$ leads to a contribution of $-26 \pm 1\text{kJ.mol}^{-1}$, which is precisely the observed energy gap in apparent activation energies. Therefore, the measured increment in activation energy was due

to a change in the degree of rate control by feeding products, in specific, a shift from an inhibitory to an irrelevant step. This behavior can also be interpreted as a change in the kinetic behavior as the dry reforming reaction approaches equilibrium, where the availability of H₂ is higher, so kinetic measurements performed at different conversion levels can lead to different interpretations of the CO₂ influence over the reaction, and even a discrepancy in the kinetic parameters.


All the evidence presented above validates the working hypothesis that oxygen is a key intermediate in the catalytic sequence of dry reforming of methane over solid solution Ni–La oxide catalysts obtained via thermal decomposition of perovskite type precursors. Indeed, the kinetic modelling showed that such an intermediate almost saturated the nickel surface and allowed the C–H bond activation of methane to occur over a metal–oxygen pair site ($\text{CH}_4 + \text{O}^* + * \rightleftharpoons \text{CH}_3^* + \text{OH}^*$) instead of a metal–metal pair site ($\text{CH}_4 + * + * \rightleftharpoons \text{CH}_3^* + \text{H}^*$) as it occurs over supported Ni catalyst.^{11,35,71,72} In this sense, we suggest that such difference is due to the Ni particle size domain and, in turn, to the presence of exposed Ni particles which are more susceptible to oxidation, i.e., a more oxophilic metal surface, caused by a poor interaction of between Ni and lanthanum oxide. The latter agrees with the fact that the CO₂ dissociates over a metal site ($\text{CO}_2^* + * \rightleftharpoons \text{CO}^* + \text{O}^*$) instead of the support (#) or interphase Ni–La₂O₃ (^{IN}) sites (**Table S8**). Therefore, the metal particle size and the metal–support interactions, which depend on the synthesis route of the catalyst, may influence the activation mechanism of the C–H and C–O bonds of both CH₄ and CO₂, respectively.

3. Conclusions

This contribution made a kinetic assessment of the dry reforming of methane reaction over a solid solution Ni–La oxide based catalyst. This material was obtained via an *in-situ* reduction of a mixture between La(OH)₃, NiO, and La₂NiO₄ phases. The reduced catalyst was composed of polycrystalline Ni particles whose average size was 220nm dispersed 0.45% over the lanthanum oxide matrix. The influence of the dry reforming reactants and products partial pressure as well as the temperature over the net CH₄, CO₂, CO, H₂ and H₂O rates was assessed after planning and executing a series of central composite statistical experiments. Based on these results and previous literature studies, seven kinetic models based on six Langmuir–Hinshelwood type reaction mechanisms were formulated and tested for describing the dry reforming reaction and the influence of the competing reverse water gas shift reaction over the catalytic behavior. Among the tested models, the one considering that the first C–H cleavage of CH₄ takes place over a metal–oxygen (*–O*) pair site described best statistically and thermodynamically the kinetic of the studied reaction system. The first C–H cleavage of the CH₄ molecule was also determined to be the rate–determining step of the reaction. A degree of rate control analysis of the model allowed establishing that the CO₂ dissociation step may inhibit the dry reforming reaction when products are absent of the reaction environment. Such behavior caused an increase in the apparent activation energy of methane and it was explained by a saturation of the surface of nickel with chemisorbed O adatoms. The results of this study help explain why solid solution Ni–La oxide catalysts perform highly and stably during methane dry reforming. Also, they provide a robust kinetic basis for the design and scale–up of the process.

AUTHOR INFORMATION

Corresponding Author

*Email: vicbaldo@uis.edu.co, Twitter: @vigabalme, Tel. +54 6344000 ext. 1485.
 <http://orcid.org/0000-0003-3227-0251>.

ASSOCIATED CONTENT

The Supporting Information includes:

Experimental methods, experimental design, assessment of mass and heat transfer limitations, estimation of the parameters of the kinetic models, and reaction mechanisms and kinetic expressions.

Author Contributions

V.S.S.-B. made the experiments, kinetic modelling and calculations, and wrote the original draft of the paper. E.M.M.-V. and C.O.C.-A. contributed revising kinetic modelling and calculations. L.M.B.-R. contributed supervising the project. V.G.B.-M. directed the project, supervised planning and execution, revised and contributed to writing the manuscript. All authors have approved the final version of the manuscript.

Notes

The authors declare no competing financial interest.

Funding Sources

This work was funded by Agencia Nacional de Hidrocarburos –ANH– and Minciencias, Colombia, within the frame of the Project 1102–721–50962: “*Desarrollo de alternativas catalíticas para la reducción y valorización de emisiones de gases de efecto invernadero típicas de pozos y refinerías petroleras por combustión catalítica de VOCs y transformación de CO₂ y CH₄ en gas de síntesis.*”

ACKNOWLEDGEMENTS

Authors thank the kind help from Laboratorio de Rayos-X-UIS under the direction of Prof. J.A Henao-Martínez for XRD analyses.

V.G.B.–M. wants to dedicate this work in commemoration to the late Prof. Aristóbulo Centeno Hurtado (1947–2011), who was his mentor and friend. Prof. Centeno was the person who introduced this author to the fascinating world of catalysis via the study of the catalytic reaction over the materials presented herein. The research featured in this paper actually came after a long pause in this research line in our group due to the always shifting budgetary priorities of the Colombian government.

REFERENCES

- (1) Zhang, G.; Liu, J.; Xu, Y.; Sun, Y. A Review of CH₄–CO₂ Reforming to Synthesis Gas over Ni-Based Catalysts in Recent Years (2010–2017). *Int. J. Hydrogen Energy* **2018**, *43* (32), 15030–15054. <https://doi.org/10.1016/j.ijhydene.2018.06.091>.
- (2) Usman, M.; Wan Daud, W. M. A.; Abbas, H. F. Dry Reforming of Methane: Influence of Process Parameters—A Review. *Renew. Sustain. Energy Rev.* **2015**, *45*, 710–744. <https://doi.org/10.1016/j.rser.2015.02.026>.
- (3) Charisiou, N. D.; Siakavelas, G.; Papageridis, K. N.; Baklavaridis, A.; Tzounis, L.; Avraam, D. G.; Goula, M. A. Syngas Production via the Biogas Dry Reforming Reaction over Nickel Supported on Modified with CeO₂ and/or La₂O₃ Alumina Catalysts. *J. Nat. Gas Sci. Eng.* **2016**, *31*, 164–183. <https://doi.org/10.1016/j.jngse.2016.02.021>.
- (4) Papadopoulou, C.; Matralis, H.; Verykios, X. Utilization of Biogas as a Renewable Carbon Source: Dry Reforming of Methane. In *Catalysis for Alternative Energy*

- Generation*; Gucci, L., Erdöhelyi, A., Eds.; Springer New York: New York, NY, 2012; pp 57–127. https://doi.org/10.1007/978-1-4614-0344-9_3.
- (5) Gili, A.; Schlicker, L.; Bekheet, M. F.; Görke, O.; Penner, S.; Grünbacher, M.; Götsch, T.; Littlewood, P.; Marks, T. J.; Stair, P. C.; Schomäcker, R.; Doran, A.; Selve, S.; Simon, U.; Gurlo, A. Surface Carbon as a Reactive Intermediate in Dry Reforming of Methane to Syngas on a 5% Ni/MnO Catalyst. *ACS Catal.* **2018**, *8* (9), 8739–8750. <https://doi.org/10.1021/acscatal.8b01820>.
- (6) Yuan, K.; Zhong, J.-Q.; Zhou, X.; Xu, L.; Bergman, S. L.; Wu, K.; Xu, G. Q.; Bernasek, S. L.; Li, H. X.; Chen, W. Dynamic Oxygen on Surface: Catalytic Intermediate and Coking Barrier in the Modeled CO₂ Reforming of CH₄ on Ni (111). *ACS Catal.* **2016**, *6* (7), 4330–4339. <https://doi.org/10.1021/acscatal.6b00357>.
- (7) Jafarbegloo, M.; Tarlani, A.; Mesbah, A. W.; Sahebdehfar, S. Thermodynamic Analysis of Carbon Dioxide Reforming of Methane and Its Practical Relevance. *Int. J. Hydrogen Energy* **2015**, *40* (6), 2445–2451. <https://doi.org/10.1016/j.ijhydene.2014.12.103>.
- (8) Challiwala, M. S.; Ghouri, M. M.; Linke, P.; El-Halwagi, M. M.; Elbashir, N. O. A Combined Thermo-Kinetic Analysis of Various Methane Reforming Technologies: Comparison with Dry Reforming. *J. CO₂ Util.* **2017**, *17*, 99–111. <https://doi.org/10.1016/j.jcou.2016.11.008>.
- (9) Dahal, A.; Bätzill, M. Graphene–Nickel Interfaces: A Review. *Nanoscale* **2014**, *6* (5), 2548. <https://doi.org/10.1039/c3nr05279f>.
- (10) Gili, A.; Schlicker, L.; Bekheet, M. F.; Görke, O.; Kober, D.; Simon, U.; Littlewood, P.; Schomäcker, R.; Doran, A.; Gaissmaier, D.; Jacob, T.; Selve, S.; Gurlo, A. Revealing the Mechanism of Multiwalled Carbon Nanotube Growth on Supported

- Nickel Nanoparticles by in Situ Synchrotron X-Ray Diffraction, Density Functional Theory, and Molecular Dynamics Simulations. *ACS Catal.* **2019**, *9* (8), 6999–7011. <https://doi.org/10.1021/acscatal.9b00733>.
- (11) Tu, W.; Ghoussoub, M.; Singh, C. V.; Chin, Y.-H. C. Consequences of Surface Oxophilicity of Ni, Ni-Co, and Co Clusters on Methane Activation. *J. Am. Chem. Soc.* **2017**, *139* (20), 6928–6945. <https://doi.org/10.1021/jacs.7b01632>.
- (12) Zhang, T.; Liu, Z.; Zhu, Y.-A.; Liu, Z.; Sui, Z.; Zhu, K.; Zhou, X. Dry Reforming of Methane on Ni-Fe-MgO Catalysts: Influence of Fe on Carbon-Resistant Property and Kinetics. *Appl. Catal. B Environ.* **2020**, *264* (February 2019), 118497. <https://doi.org/10.1016/j.apcatb.2019.118497>.
- (13) Gonzalez-DelaCruz, V. M.; Holgado, J. P.; Pereñíguez, R.; Caballero, A. Morphology Changes Induced by Strong Metal-Support Interaction on a Ni-Ceria Catalytic System. *J. Catal.* **2008**, *257* (2), 307–314. <https://doi.org/10.1016/j.jcat.2008.05.009>.
- (14) Han, J. W.; Park, J. S.; Choi, M. S.; Lee, H. Uncoupling the Size and Support Effects of Ni Catalysts for Dry Reforming of Methane. *Appl. Catal. B Environ.* **2017**, *203*, 625–632. <https://doi.org/10.1016/j.apcatb.2016.10.069>.
- (15) Wu, P.; Tao, Y.; Ling, H.; Chen, Z.; Ding, J.; Zeng, X.; Liao, X.; Stampfl, C.; Huang, J. Cooperation of Ni and CaO at Interface for CO₂ Reforming of CH₄: A Combined Theoretical and Experimental Study. *ACS Catal.* **2019**, *9* (11), 10060–10069. <https://doi.org/10.1021/acscatal.9b02286>.
- (16) Zhang, Z.; Verykios, X. Carbon Dioxide Reforming of Methane to Synthesis Gas over Ni/La₂O₃ Catalysts. *Appl. Catal. A Gen.* **1996**, *138* (1), 109–133. [https://doi.org/10.1016/0926-860X\(95\)00238-3](https://doi.org/10.1016/0926-860X(95)00238-3).

- (17) Bonmassar, N.; Bekheet, M. F.; Schlicker, L.; Gili, A.; Gurlo, A.; Doran, A.; Gao, Y.; Heggen, M.; Bernardi, J.; Klötzer, B.; Penner, S. In Situ-Determined Catalytically Active State of LaNiO₃ in Methane Dry Reforming. *ACS Catal.* **2020**, *10* (2), 1102–1112. <https://doi.org/10.1021/acscatal.9b03687>.
- (18) Faroldi, B. M.; Múnera, J. F.; Cornaglia, L. M. In Situ Characterization of Phase Transformation and Reactivity of High Surface Area Lanthanum-Based Ru Catalysts for the Combined Reforming of Methane. *Appl. Catal. B Environ.* **2014**, *150–151*, 126–137. <https://doi.org/10.1016/j.apcatb.2013.12.005>.
- (19) Slagtern, A.; Schuurman, Y.; Leclercq, C.; Verykios, X.; Mirodatos, C. Specific Features Concerning the Mechanism of Methane Reforming by Carbon Dioxide over Ni/La₂O₃ Catalyst. *J. Catal.* **1997**, *172* (1), 118–126. <https://doi.org/10.1006/jcat.1997.1823>.
- (20) Osazuwa, O. U.; Setiabudi, H. D.; Abdullah, S.; Cheng, C. K. Syngas Production from Methane Dry Reforming over SmCoO₃ Perovskite Catalyst: Kinetics and Mechanistic Studies. *Int. J. Hydrogen Energy* **2017**, *42* (15), 9707–9721. <https://doi.org/10.1016/j.ijhydene.2017.03.061>.
- (21) Manoilova, O. V.; Podkolzin, S. G.; Tope, B.; Lercher, J.; Stangland, E. E.; Goupil, J.-M.; Weckhuysen, B. M. Surface Acidity and Basicity of La₂O₃, LaOCl, and LaCl₃ Characterized by IR Spectroscopy, TPD, and DFT Calculations. *J. Phys. Chem. B* **2004**, *108* (40), 15770–15781. <https://doi.org/10.1021/jp040311m>.
- (22) Wang, S.; Cong, L.; Zhao, C.; Li, Y.; Pang, Y.; Zhao, Y.; Li, S.; Sun, Y. First Principles Studies of CO₂ and O₂ Chemisorption on La₂O₃ Surfaces. *Phys. Chem. Chem. Phys.* **2017**, *19* (39), 26799–26811. <https://doi.org/10.1039/C7CP05471H>.
- (23) Singh, S.; Zubenko, D.; Rosen, B. A. Influence of LaNiO₃ Shape on Its Solid-Phase

- Crystallization into Coke-Free Reforming Catalysts. *ACS Catal.* **2016**, *6* (7), 4199–4205. <https://doi.org/10.1021/acscatal.6b00673>.
- (24) Singh, S.; Prestat, E.; Huang, L.-F.; Rondinelli, J. M.; Haigh, S. J.; Rosen, B. A. Role of 2D and 3D Defects on the Reduction of LaNiO₃ Nanoparticles for Catalysis. *Sci. Rep.* **2017**, *7* (1), 10080. <https://doi.org/10.1038/s41598-017-10703-5>.
- (25) Tsipouriari, V.; Verykios, X. Carbon and Oxygen Reaction Pathways of CO₂ Reforming of Methane over Ni/La₂O₃ and Ni/Al₂O₃ Catalysts Studied by Isotopic Tracing Techniques. *J. Catal.* **1999**, *94*, 85–94.
- (26) Argyle, M. D.; Bartholomew, C. H. Heterogeneous Catalyst Deactivation and Regeneration: A Review. *Catalysts* **2015**, *5* (1), 145–269. <https://doi.org/10.3390/catal5010145>.
- (27) Kim, J.-W.; Ha, J.-A.; Jung, H.; Ahn, B.-I.; Lee, S.-H.; Choi, J.-G. Kinetic Analysis of Supported Ni-Catalyzed CO₂/CH₄ Reactions Using Photoacoustic Spectroscopy. *Phys. Chem. Chem. Phys.* **2007**, *9* (43), 5828. <https://doi.org/10.1039/b709102h>.
- (28) Bradford, M. C. J.; Vannice, M. A. Catalytic Reforming of Methane with Carbon Dioxide over Nickel Catalysts II. Reaction Kinetics. *Appl. Catal. A Gen.* **1996**, *142* (1), 97–122. [https://doi.org/10.1016/0926-860X\(96\)00066-X](https://doi.org/10.1016/0926-860X(96)00066-X).
- (29) Sierra-Gallego, G.; Batiot-Dupeyrat, C.; Barrault, J.; Mondragón, F. Dual Active-Site Mechanism for Dry Methane Reforming over Ni/La₂O₃ Produced from LaNiO₃ Perovskite. *Ind. Eng. Chem. Res.* **2008**, *47* (23), 9272–9278. <https://doi.org/10.1021/ie800281t>.
- (30) Verykios, X. Catalytic Dry Reforming of Natural Gas for the Production of Chemicals and Hydrogen. *Int. J. Hydrogen Energy* **2003**, *28* (10), 1045–1063. [https://doi.org/10.1016/S0360-3199\(02\)00215-X](https://doi.org/10.1016/S0360-3199(02)00215-X).

- (31) Bobrova, L. N.; Bobin, A. S.; Mezentseva, N. V.; Sadykov, V. A.; Thybaut, J. W.; Marin, G. B. Kinetic Assessment of Dry Reforming of Methane on Pt + Ni Containing Composite of Fluorite-like Structure. *Appl. Catal. B Environ.* **2016**, *182*, 513–524. <https://doi.org/10.1016/j.apcatb.2015.09.049>.
- (32) Zhang, J.; Wang, H.; Dalai, A. K. Kinetic Studies of Carbon Dioxide Reforming of Methane over Ni–Co/Al–Mg–O Bimetallic Catalyst. *Ind. Eng. Chem. Res.* **2009**, *48* (2), 677–684. <https://doi.org/10.1021/ie801078p>.
- (33) Pichas, C.; Pomonis, P.; Petrakis, D.; Ladavos, A. Kinetic Study of the Catalytic Dry Reforming of CH₄ with CO₂ over La_{2–x}Sr_xNiO₄ Perovskite-Type Oxides. *Appl. Catal. A Gen.* **2010**, *386* (1–2), 116–123. <https://doi.org/10.1016/j.apcata.2010.07.043>.
- (34) Kathiraser, Y.; Oemar, U.; Saw, E. T.; Li, Z.; Kawi, S. Kinetic and Mechanistic Aspects for CO₂ Reforming of Methane over Ni Based Catalysts. *Chem. Eng. J.* **2015**, *278*, 62–78. <https://doi.org/10.1016/j.cej.2014.11.143>.
- (35) Tsipouriari, V.; Verykios, X. Kinetic Study of the Catalytic Reforming of Methane with Carbon Dioxide to Synthesis Gas over Ni/La₂O₃ Catalyst. *Catal. Today* **2001**, *64* (1–2), 83–90. [https://doi.org/10.1016/S0920-5861\(00\)00511-3](https://doi.org/10.1016/S0920-5861(00)00511-3).
- (36) Fan, C.; Zhu, Y.-A.; Yang, M.-L.; Sui, Z.-J.; Zhou, X.-G.; Chen, D. Density Functional Theory-Assisted Microkinetic Analysis of Methane Dry Reforming on Ni Catalyst. *Ind. Eng. Chem. Res.* **2015**, *54* (22), 5901–5913. <https://doi.org/10.1021/acs.iecr.5b00563>.
- (37) Moradi, G. R.; Rahmanzadeh, M.; Sharifnia, S. Kinetic Investigation of CO₂ Reforming of CH₄ over La–Ni Based Perovskite. *Chem. Eng. J.* **2010**, *162* (2), 787–791. <https://doi.org/10.1016/j.cej.2010.06.006>.

- (38) Múnera, J. F.; Irusta, S.; Cornaglia, L. M.; Lombardo, E. A.; Vargas Cesar, D.; Schmal, M. Kinetics and Reaction Pathway of the CO₂ reforming of Methane on Rh Supported on Lanthanum-Based Solid. *J. Catal.* **2007**, *245* (1), 25–34.
<https://doi.org/10.1016/j.jcat.2006.09.008>.
- (39) Boudart, M.; Djega-Mariadassou, G. *Kinetics of Heterogeneous Catalytic Reactions*, 1st ed.; Princeton University Press: Princeton, 1984.
- (40) Vannice, M. A.; Hyun, S.; Kalpakci, B.; Liauh, W. Entropies of Adsorption in Heterogeneous Catalytic Reactions. *J. Catal.* **1979**, *56* (3), 358–362.
[https://doi.org/10.1016/0021-9517\(79\)90128-3](https://doi.org/10.1016/0021-9517(79)90128-3).
- (41) Dehimi, L.; Benguerba, Y.; Virginie, M.; Hijazi, H. Microkinetic Modelling of Methane Dry Reforming over Ni/Al₂O₃ Catalyst. *Int. J. Hydrogen Energy* **2017**, *42* (30), 18930–18940. <https://doi.org/10.1016/j.ijhydene.2017.05.231>.
- (42) Benguerba, Y.; Dehimi, L.; Virginie, M.; Dumas, C.; Ernst, B. Modelling of Methane Dry Reforming over Ni/Al₂O₃ Catalyst in a Fixed-Bed Catalytic Reactor. *React. Kinet. Mech. Catal.* **2015**, *114* (1), 109–119. <https://doi.org/10.1007/s11144-014-0772-5>.
- (43) Abbas, S. Z.; Dupont, V.; Mahmud, T. Kinetics Study and Modelling of Steam Methane Reforming Process over a NiO/Al₂O₃ Catalyst in an Adiabatic Packed Bed Reactor. *Int. J. Hydrogen Energy* **2017**, *42* (5), 2889–2903.
<https://doi.org/10.1016/j.ijhydene.2016.11.093>.
- (44) Baldovino-Medrano, V. G.; Pérez-Martínez, D. de J.; Giraldo, S.-A.; Centeno, A. *Reformado de Metano Con CO₂ Sobre Catalizadores Ni/La₂O₃ Obtenidos a Partir de La Perovskita LaNiO₃*, 1st ed.; Academica de Catálisis: Mérida, 2004.
- (45) Baldovino-Medrano, V. G.; Pérez-Martínez, D. de J. Reformado de Metano Con

CO₂ Sobre Catalizadores Ni/La₂O₃ Obtenidos a Partir de La Perovskita LaNiO₃,
Universidad Industrial de Santander, Bucaramanga, 2003.

- (46) Sandoval Bohórquez, V. S.; Peña Prada, J. A.; Pérez-Martínez, D. de J.; Baldovino-Medrano, V. G. Reformado de Metano Con CO₂ Sobre Catalizadores Ni/La₂O₃ Obtenidos a Partir de La Perovskita LaNiO₃. In *Memorias del X Simposio Colombiano de Catálisis*; Universidad Pedagógica y Tecnológica de Colombia: Tunja, 2017. [https://doi.org/ISSN: 2619-6042](https://doi.org/ISSN:2619-6042).
- (47) Dorofeev, G. A.; Streletskii, A. N.; Povstugar, I. V.; Protasov, A. V.; Elsukov, E. P. Determination of Nanoparticle Sizes by X-Ray Diffraction. *Colloid J.* **2012**, *74* (6), 675–685. <https://doi.org/10.1134/S1061933X12060051>.
- (48) Bandrowski, J.; Bickling, C. R.; Yang, K. H.; Hougen, O. A. Kinetics of the Reduction of Nickel Oxide by Hydrogen. *Chem. Eng. Sci.* **1962**, *17* (5), 379–390. [https://doi.org/10.1016/0009-2509\(62\)80039-6](https://doi.org/10.1016/0009-2509(62)80039-6).
- (49) Szekely, J.; Lin, C. I.; Sohn, H. Y. A Structural Model for Gas—Solid Reactions with a Moving Boundary—V an Experimental Study of the Reduction of Porous Nickel-Oxide Pellets with Hydrogen. *Chem. Eng. Sci.* **1973**, *28* (11), 1975–1989. [https://doi.org/10.1016/0009-2509\(73\)85042-0](https://doi.org/10.1016/0009-2509(73)85042-0).
- (50) Ino, E.; Shimizu, K.; Yamate, T. Studies on Thermal Decomposition Process of Lanthanum Hydroxide. *J. Soc. Mater. Sci. Japan* **1976**, *25* (279), 1165–1168. <https://doi.org/10.2472/jsms.25.1165>.
- (51) Haibel, E.; Berendts, S.; Walter, D. Thermogravimetric and X-Ray Diffraction Investigation on Carbonated Lanthanum Oxide and Lanthanum Hydroxide Formed in Humid CO₂ Atmosphere. *J. Therm. Anal. Calorim.* **2018**, *134* (1), 261–267. <https://doi.org/10.1007/s10973-018-7256-1>.

- (52) Fontaine, M.-L.; Laberty-Robert, C.; Ansart, F.; Tailhades, P. Elaboration and Characterization of $\text{La}_2\text{NiO}_{4+\delta}$ Powders and Thin Films via a Modified Sol–Gel Process. *J. Solid State Chem.* **2004**, *177* (4–5), 1471–1479. <https://doi.org/10.1016/j.jssc.2003.11.032>.
- (53) Manukyan, K. V.; Avetisyan, A. G.; Shuck, C. E.; Chatilyan, H. A.; Rouvimov, S.; Kharatyan, S. L.; Mukasyan, A. S. Nickel Oxide Reduction by Hydrogen: Kinetics and Structural Transformations. *J. Phys. Chem. C* **2015**, *119* (28), 16131–16138. <https://doi.org/10.1021/acs.jpcc.5b04313>.
- (54) Sierra Gallego, G.; Mondragón, F.; Tatibouët, J.-M.; Barrault, J.; Batiot-Dupeyrat, C. Carbon Dioxide Reforming of Methane over La_2NiO_4 as Catalyst Precursor— Characterization of Carbon Deposition. *Catal. Today* **2008**, *133–135* (1–4), 200–209. <https://doi.org/10.1016/j.cattod.2007.12.075>.
- (55) Choisnet, J.; Abadzhieva, N.; Stefanov, P.; Klissurski, D.; Bassat, J. M.; Rives, V.; Minchev, L. X-Ray Photoelectron Spectroscopy, Temperature-Programmed Desorption and Temperature-Programmed Reduction Study of LaNiO_3 and La_2NiO_4 Catalysts for Methanol Oxidation. *J. Chem. Soc. Faraday Trans.* **1994**, *90* (13), 1987. <https://doi.org/10.1039/ft9949001987>.
- (56) Thommes, M.; Kaneko, K.; Neimark, A. V.; Olivier, J. P.; Rodriguez-Reinoso, F.; Rouquerol, J.; Sing, K. S. W. Physisorption of Gases, with Special Reference to the Evaluation of Surface Area and Pore Size Distribution (IUPAC Technical Report). *Pure Appl. Chem.* **2015**, *87* (9–10), 1051–1069. <https://doi.org/10.1515/pac-2014-1117>.
- (57) Huízar-Félix, A. M.; Hernández, T.; de la Parra, S.; Ibarra, J.; Kharisov, B. Sol–Gel Based Pechini Method Synthesis and Characterization of $\text{Sm}_{1-x}\text{Ca}_x\text{FeO}_3$

Perovskite $0.1 \leq x \leq 0.5$. *Powder Technol.* **2012**, 229, 290–293.

<https://doi.org/10.1016/j.powtec.2012.06.057>.

- (58) Sunde, T. O. L.; Grande, T.; Einarsrud, M.-A. Modified Pechini Synthesis of Oxide Powders and Thin Films. In *Handbook of Sol-Gel Science and Technology*; Springer International Publishing: Cham, 2016; pp 1–30. https://doi.org/10.1007/978-3-319-19454-7_130-1.
- (59) Vargas, M. A.; Diosa, J. E.; Mosquera, E. The Structural, Optical and Magnetic Property of Iron Oxides Submicron Particles Synthesized by the Pechini Method from Steel Industry Wastes. *J. Magn. Magn. Mater.* **2020**, 513, 167243. <https://doi.org/10.1016/j.jmmm.2020.167243>.
- (60) Bergeret, G.; Gallezot, P. Particle Size and Dispersion Measurements. In *Handbook of Heterogeneous Catalysis*; Wiley-VCH Verlag GmbH & Co. KGaA: Weinheim, Germany, 2008. <https://doi.org/10.1002/9783527610044.hetcat0038>.
- (61) Ro, I.; Resasco, J.; Christopher, P. Approaches for Understanding and Controlling Interfacial Effects in Oxide-Supported Metal Catalysts. *ACS Catal.* **2018**, 8 (8), 7368–7387. <https://doi.org/10.1021/acscatal.8b02071>.
- (62) Li, K.; Chang, X.; Pei, C.; Li, X.; Chen, S.; Zhang, X.; Assabumrungrat, S.; Zhao, Z.-J.; Zeng, L.; Gong, J. Ordered Mesoporous Ni/La₂O₃ Catalysts with Interfacial Synergism towards CO₂ Activation in Dry Reforming of Methane. *Appl. Catal. B Environ.* **2019**, 259 (May), 118092. <https://doi.org/10.1016/j.apcatb.2019.118092>.
- (63) Zhang, Z.; Verykios, X. E. A Stable and Active Nickel-Based Catalyst for Carbon Dioxide Reforming of Methane to Synthesis Gas. *J. Chem. Soc. Chem. Commun.* **1995**, No. 1, 71. <https://doi.org/10.1039/c39950000071>.
- (64) Batiot-Dupeyrat, C.; Sierra Gallego, G. A.; Mondragon, F.; Barrault, J.; Tatibouët,

- J.-M. CO₂ Reforming of Methane over LaNiO₃ as Precursor Material. *Catal. Today* **2005**, *107–108*, 474–480. <https://doi.org/10.1016/j.cattod.2005.07.014>.
- (65) Sierra Gallego, G.; Mondragón, F.; Barrault, J.; Tatibouët, J.-M.; Batiot-Dupeyrat, C. CO₂ Reforming of CH₄ over La–Ni Based Perovskite Precursors. *Appl. Catal. A Gen.* **2006**, *311*, 164–171. <https://doi.org/10.1016/j.apcata.2006.06.024>.
- (66) Rivas, I.; Alvarez, J.; Pietri, E.; Pérez-Zurita, M. J.; Goldwasser, M. R. Perovskite-Type Oxides in Methane Dry Reforming: Effect of Their Incorporation into a Mesoporous SBA-15 Silica-Host. *Catal. Today* **2010**, *149* (3–4), 388–393. <https://doi.org/10.1016/j.cattod.2009.05.028>.
- (67) Pereñiguez, R.; Gonzalez-delaCruz, V. M.; Caballero, A.; Holgado, J. P. LaNiO₃ as a Precursor of Ni/La₂O₃ for CO₂ Reforming of CH₄: Effect of the Presence of an Amorphous NiO Phase. *Appl. Catal. B Environ.* **2012**, *123–124*, 324–332. <https://doi.org/10.1016/j.apcatb.2012.04.044>.
- (68) Messaoudi, H.; Thomas, S.; Djaidja, A.; Slyemi, S.; Barama, A. Study of LaxNiO y and LaxNiO/MgAl₂O₄ Catalysts in Dry Reforming of Methane. *J. CO₂ Util.* **2018**, *24* (December 2017), 40–49. <https://doi.org/10.1016/j.jcou.2017.12.002>.
- (69) Bhore, N. A.; Klein, M. T.; Bischoff, K. B. The Delplot Technique: A New Method for Reaction Pathway Analysis. *Ind. Eng. Chem. Res.* **1990**, *29* (2), 313–316. <https://doi.org/10.1021/ie00098a025>.
- (70) Chin, Y.-H. (Cathy); Buda, C.; Neurock, M.; Iglesia, E. Consequences of Metal–Oxide Interconversion for C–H Bond Activation during CH₄ Reactions on Pd Catalysts. *J. Am. Chem. Soc.* **2013**, *135* (41), 15425–15442. <https://doi.org/10.1021/ja405004m>.
- (71) Wei, J.; Iglesia, E. Isotopic and Kinetic Assessment of the Mechanism of Reactions

- of CH₄ with CO₂ or H₂O to Form Synthesis Gas and Carbon on Nickel Catalysts. *J. Catal.* **2004**, *224* (2), 370–383. <https://doi.org/10.1016/j.jcat.2004.02.032>.
- (72) Wei, J.; Iglesia, E. Mechanism and Site Requirements for Activation and Chemical Conversion of Methane on Supported Pt Clusters and Turnover Rate Comparisons among Noble Metals. *J. Phys. Chem. B* **2004**, *108* (13), 4094–4103. <https://doi.org/10.1021/jp036985z>.
- (73) Li, K.; He, F.; Yu, H.; Wang, Y.; Wu, Z. Theoretical Study on the Reaction Mechanism of Carbon Dioxide Reforming of Methane on La and La₂O₃ Modified Ni(111) Surface. *J. Catal.* **2018**, *364*, 248–261. <https://doi.org/10.1016/j.jcat.2018.05.026>.
- (74) Xie, Z.; Liao, Q.; Liu, M.; Yang, Z.; Zhang, L. Micro-Kinetic Modeling Study of Dry Reforming of Methane over the Ni-Based Catalyst. *Energy Convers. Manag.* **2017**, *153* (August), 526–537. <https://doi.org/10.1016/j.enconman.2017.10.022>.
- (75) Caballero, K. V; Guerrero-Amaya, H.; Baldovino-Medrano, V. G. Revisiting Glycerol Esterification with Acetic Acid over Amberlyst-35 via Statistically Designed Experiments: Overcoming Transport Limitations. *Chem. Eng. Sci.* **2019**. <https://doi.org/https://doi.org/10.1016/j.ces.2019.06.003>.
- (76) Zuo, Z.; Liu, S.; Wang, Z.; Liu, C.; Huang, W.; Huang, J.; Liu, P. Dry Reforming of Methane on Single-Site Ni/MgO Catalysts: Importance of Site Confinement. *ACS Catal.* **2018**, *8* (10), 9821–9835. <https://doi.org/10.1021/acscatal.8b02277>.
- (77) Zhu, Y. A.; Chen, D.; Zhou, X. G.; Yuan, W. K. DFT Studies of Dry Reforming of Methane on Ni Catalyst. *Catal. Today* **2009**, *148* (3–4), 260–267. <https://doi.org/10.1016/j.cattod.2009.08.022>.
- (78) Gallego, J.; Sierra-Gallego, G.; Tapia, J.; Mondragón, F.; Batiot-Dupeyrat, C.

- Activation of CO₂ on Ni/La₂O₃: Non-Isothermal Kinetic Study on the Basis of Thermogravimetric Studies. *React. Kinet. Mech. Catal.* **2016**, *119* (1), 179–193.
<https://doi.org/10.1007/s11144-016-1032-7>.
- (79) Bai, Y.; Kirvassilis, D.; Xu, L.; Mavrikakis, M. Atomic and Molecular Adsorption on Ni(111). *Surf. Sci.* **2019**, *679* (June 2018), 240–253.
<https://doi.org/10.1016/j.susc.2018.08.004>.
- (80) Herrera, K.; Maier, L.; Tischer, S.; Zellner, A.; Stotz, H.; Deutschmann, O. Surface Reaction Kinetics of Steam- and CO₂-Reforming as Well as Oxidation of Methane over Nickel-Based Catalysts. *Catalysts* **2015**, *5* (2), 871–904.
<https://doi.org/10.3390/catal5020871>.
- (81) Rajkhowa, T.; Marin, G. B.; Thybaut, J. W. A Comprehensive Kinetic Model for Cu Catalyzed Liquid Phase Glycerol Hydrogenolysis. *Appl. Catal. B Environ.* **2017**, *205*, 469–480. <https://doi.org/10.1016/j.apcatb.2016.12.042>.
- (82) Otyuskaya, D.; Thybaut, J. W.; Alexiadis, V.; Alekseeva, M.; Venderbosch, R.; Yakovlev, V.; Marin, G. B. Fast Pyrolysis Oil Stabilization Kinetics over a Ni-Cu Catalyst Using Propionic Acid as a Model Compound. *Appl. Catal. B Environ.* **2018**, *233* (March), 46–57. <https://doi.org/10.1016/j.apcatb.2018.03.062>.
- (83) Santacesaria, E. Kinetics and Transport Phenomena. *Catal. Today* **1997**, *34* (3–4), 393–400. [https://doi.org/10.1016/S0920-5861\(96\)00061-2](https://doi.org/10.1016/S0920-5861(96)00061-2).
- (84) Çengel, Y. A.; Boles, M. A. *Thermodynamics: An Engineering Approach*, 8th ed.; McGraw-Hill Education: New York, NY, 2015.
- (85) Dumesic, J. A.; Rudd, D. F.; Aparicio, L. M.; Rekoske, J. E.; Treviño, A. A. *The Microkinetics of Heterogeneous Catalysis*; American Chemical Society: Washington DC, 1993.

- (86) Campbell, C. T.; Árnadóttir, L.; Sellers, J. R. V. Kinetic Prefactors of Reactions on Solid Surfaces. *Zeitschrift für Phys. Chemie* **2013**, *227* (9–11), 1435–1454.
<https://doi.org/10.1524/zpch.2013.0395>.
- (87) Foppa, L.; Margossian, T.; Kim, S. M.; Müller, C.; Copéret, C.; Larmier, K.; Comas-Vives, A. Contrasting the Role of Ni/Al₂O₃ Interfaces in Water–Gas Shift and Dry Reforming of Methane. *J. Am. Chem. Soc.* **2017**, *139* (47), 17128–17139.
<https://doi.org/10.1021/jacs.7b08984>.
- (88) Han, Z.; Yang, Z.; Han, M. Comprehensive Investigation of Methane Conversion over Ni(111) Surface under a Consistent DFT Framework: Implications for Anti-Coking of SOFC Anodes. *Appl. Surf. Sci.* **2019**, *480* (February), 243–255.
<https://doi.org/10.1016/j.apsusc.2019.02.084>.
- (89) Harris, J. W.; Verma, A. A.; Arvay, J. W.; Shih, A. J.; Delgass, W. N.; Ribeiro, F. H. Consequences of Product Inhibition in the Quantification of Kinetic Parameters. *J. Catal.* **2020**, *389*, 468–475. <https://doi.org/10.1016/j.jcat.2020.06.014>.
- (90) Jørgensen, M.; Grönbeck, H. Connection between Macroscopic Kinetic Measurables and the Degree of Rate Control. *Catal. Sci. Technol.* **2017**, *7* (18), 4034–4040.
<https://doi.org/10.1039/C7CY01246B>.
- (91) Mao, Z.; Campbell, C. T. Apparent Activation Energies in Complex Reaction Mechanisms: A Simple Relationship via Degrees of Rate Control. *ACS Catal.* **2019**, *9* (10), 9465–9473. <https://doi.org/10.1021/acscatal.9b02761>.